bioRxiv preprint doi: https://doi.org/10.1101/2023.03.07.531595; this version posted March 7, 2023. The copyright holder for this preprint (which was not certified by peer review) is the author/funder. All rights reserved. No reuse allowed without permission.

Bsc2 is a novel regulator of triglyceride lipolysis that demarcates a lipid droplet subpopulation

Authors: Natalie Ortiz Speer[1], R. Jay Braun[2], Emma Grace Reynolds[1], Jessica M.J. Swanson[2], W. Mike Henne[1]

*correspondence: mike.henne@utsouthwestern.edu

Affiliations:

[1]Department of Cell Biology, UT Southwestern Medical Center, Dallas, TX 75390, USA

[2]Department of Chemistry, University of Utah, Salt Lake City, UT 84112, USA

Abstract:

Cells store lipids in the form of triglyceride (TG) and sterol-ester (SE) in lipid droplets (LDs). Distinct pools of LDs exist, but a pervasive question is how proteins localize to and convey functions to LD subsets. Here, we show the yeast protein Bsc2 localizes to a subset of TG-containing LDs, and reveal it negatively regulates TG lipolysis. Mechanistically, Bsc2 LD targeting requires TG, and LD targeting is mediated by hydrophobic regions (HRs). Molecular dynamics simulations reveal these Bsc2 HRs interact with TG on modeled LDs, and adopt specific conformations on TG-rich LDs versus SE-rich LDs or an ER bilayer. Bsc2-deficient yeast display no defect in LD biogenesis, but exhibit elevated TG lipolysis dependent on lipase Tgl3. Remarkably, Bsc2 abundance influences TG, and over-expression of Bsc2, but not LD protein Pln1, promotes TG accumulation without altering SE. Finally, we find Bsc2-deficient cells display altered LD mobilization during stationary growth. We propose Bsc2 regulates lipolysis and localizes to subsets of TG-enriched LDs.

Key words:

Lipid droplet (LD); triglyceride (TG); sterol-ester (SE); lipolysis; molecular dynamics simulation; LD protein targeting

bioRxiv preprint doi: https://doi.org/10.1101/2023.03.07.531595; this version posted March 7, 2023. The copyright holder for this preprint (which was not certified by peer review) is the author/funder. All rights reserved. No reuse allowed without permission.

Introduction:

Lipid droplets (LDs) are fat storage organelles comprised of a neutral lipid core containing both triglycerides (TG) and sterol esters (SE) (Walther et al., 2017). Distinct from bilayer-bound organelles, LDs are surrounded by a phospholipid (PL) monolayer which is decorated with surface proteins that aid in their biogenesis and degradation (Currie et al., 2014). These cytosolic lipid reservoirs can be made or broken down in response to a variety of metabolic cues, such as nutrient deprivation or increased membrane biogenesis. Defects in lipid storage in LDs contribute to numerous metabolic disorders including obesity, cardiovascular disease, and diabetes (Welte, 2015; Gluchowski et al., 2017). Recent studies indicate that beyond their role in lipid storage, LDs also play important roles in signaling and protein homeostasis (Li et al., 2012; Bersuker et al., 2018; Schmeisser et al., 2019). Despite this, it remains unclear if distinct pools of LDs exist within cells to enable this functional diversity. Work from our group and others have shown that LDs are not homogenous within the context of a single cell, but exist in a variety of subpopulations that contain distinct proteomes and/or morphologies (Zhang et al., 2016; Eisenberg-Bord et al., 2018; Teixeira et al., 2018; Schott et al., 2019; Ugrankar et al., 2019). Although LDs exhibit these unique features, little is currently known regarding how such differences dictate LD function. LD subpopulations are of particular interest to the field of metabolism as there is mounting evidence that different LD pools play roles in maintaining metabolic homeostasis in response to various nutrient states (Hariri et al., 2018; Eisenberg-Bord et al., 2018; Teixeira et al., 2018). For example, large and small LD pools observed in human hepatocytes are mobilized by mechanistically distinct pathways during starvation (Schott et al., 2019). Similarly, *Drosophila* fat body cells contain two subpopulations of LDs that are differentially maintained by extracellular and *de novo* synthesis of lipids (Ugrankar et al., 2019).

LD turnover primarily occurs through a highly conserved process known as lipolysis. This catabolic process involves the targeting of cytoplasmic lipases to LDs where they hydrolyze TG and SE to base components. TG breakdown via lipolysis is necessary for maintaining lipid homeostasis, sustaining membrane biosynthesis, and promoting

bioRxiv preprint doi: https://doi.org/10.1101/2023.03.07.531595; this version posted March 7, 2023. The copyright holder for this preprint (which was not certified by peer review) is the author/funder. All rights reserved. No reuse allowed without permission.

cellular division across multiple species (Duncan et al., 2007; Schmidt et al., 2014; Heier and Kühnlein, 2018). However, the underlying mechanisms for regulation of TG lipolysis in budding yeast are poorly understood. Yeast contain three LD-resident and paralogous TG lipases: Tgl3, Tgl4, and Tgl5 (Athenstaedt et al., 1999; Athenstaedt and Daum, 2003, 2005; Kurat et al., 2006). Although Tgl4 has been shown to be the functional ortholog of the mammalian TG lipase, ATGL, in yeast, it is in fact Tgl3 that performs the bulk of the lipolytic activity *in vivo* as it can hydrolyze TG species of variable fatty acid chain length (Athenstaedt and Daum, 2003, 2005; Kurat et al., 2006). The regulation of Tgl3-mediated TG lipolysis is poorly understood. Previous studies provide some insight by demonstrating that in the absence of either TG or LDs as whole, Tgl3 activity, targeting, and stability is negatively impacted, a common trait for many resident LD proteins (Schmidt et al., 2013; Koch et al., 2014). In LD-null yeast, Tgl3 is re-targeted to the ER where it loses its lipolytic activity and is rapidly degraded (Schmidt et al., 2013). In spite of this information, specific regulators of Tgl3 TG lipase activity remain unidentified. Whether specific LD subsets are preferentially mobilized during metabolic cues is also underexplored.

Here, we deorphanize and characterize the LD protein Bsc2 as a negative regulator of TG lipolysis in yeast. We show that Bsc2 enriches on a subpopulation of LDs at logarithmic (LOG) phase yeast growth. We find Bsc2 LD targeting is dependent on the presence of TG, as Bsc2 fails to stably localize to SE-LDs. Structure-function analysis reveals the N-terminal half of Bsc2, containing distinct hydrophobic domains, is necessary for stable LD association. This is supported by molecular dynamics (MD) simulations that demonstrate Bsc2 adopts a distinct conformational ensemble on TG-rich LDs and interacts extensively with TG in addition to LD monolayer PLs. Physiologically, loss of Bsc2 (*bsc2*Δ) generates a significant decrease in steady-state TG during yeast LOG phase growth. We show this decrease is not due to reduced TG synthesis, but rather from upregulated Tgl3-dependent TG lipolysis. Notably, Bsc2 over-expression promotes TG accumulation and LD enlargement in yeast, but does not alter SE pools. We propose that Bsc2 demarcates a LD subpopulation, where it locally inhibits Tgl3-dependent TG lipolysis.

bioRxiv preprint doi: https://doi.org/10.1101/2023.03.07.531595; this version posted March 7, 2023. The copyright holder for this preprint (which was not certified by peer review) is the author/funder. All rights reserved. No reuse allowed without permission.

Results:

Bsc2 localizes to a LD subset and requires TG for LD targeting

To dissect how proteins target to specific lipid droplets (LD) subpopulations, we used a candidate-based approach to image GFP-tagged proteins annotated to localize to LDs in the budding yeast *Saccharomyces cerevisiae*. We manually imaged yeast expressing these chromosomally GFP-tagged proteins and co-expressing the canonical LD protein Erg6-mRuby, a previously established LD marker known to decorate all yeast LDs (Müllner et al., 2004). Candidate-based imaging revealed that Bsc2-GFP, a canonical LD targeting protein of unknown function, was detected on only a subset of Erg6-mRuby labeled LDs in yeast growing at logarithmic (LOG) phase (**Fig 1A**). Similarly, LOG-phase yeast expressing Bsc2-GFP and stained with the general LD dye monodansylpentane (MDH) also showed partial MDH and Bsc2-GFP co-localization (**Fig 1C**). Consistent with this, previous work also determined that Bsc2 was among a few LD proteins detected on only LD subsets in budding yeast (Eisenberg-Bord et al., 2018; Teixeira et al., 2018). To determine whether Bsc2-GFP decorated a LD subset in yeast in different growth phases, we also imaged yeast grown into stationary (STAT) phase, when cell growth slows and LD lipid storage is elevated. STAT phase yeast also exhibited detectable Bsc2-GFP on LDs, but this Bsc2-GFP signal colocalized closely with Erg6-mRuby (**Fig 1A**). Quantification of this Bsc2-GFP/Erg6-mRuby colocalization in LOG and STAT phases revealed that in LOG phase, only ~40% of Erg6-mRuby LDs also exhibited detectable Bsc2-GFP (**Fig 1B**). In STAT phase this detectable co-localization increased to ~70%, suggesting Bsc2-GFP and Erg6-mRuby colocalization increased in STAT phase.

Recent work indicates that LD neutral lipid composition can influence protein targeting to the LD surface (Thiam and Beller, 2017; Chorlay and Thiam, 2020; Caillon et al., 2020; Dhiman et al., 2020). Since yeast LDs contain TG and SE, we next dissected whether loss of either of these neutral lipids influenced Bsc2-mNeonGreen (Bsc2-mNG) LD localization. We generated a chromosomally-tagged Bsc2-mNG yeast strain that produced only TG (TG-only) by deleting the genes encoding the two SE-generating

bioRxiv preprint doi: https://doi.org/10.1101/2023.03.07.531595; this version posted March 7, 2023. The copyright holder for this preprint (which was not certified by peer review) is the author/funder. All rights reserved. No reuse allowed without permission.

enzymes Are1 and Are2, and a strain producing only SEs (SE-only) by deleting the TG-synthesis enzymes Dga1 and Lro1 (Sandager et al., 2002; Sorger et al., 2004). Imaging revealed that whereas the wildtype (WT) and TG-only yeast exhibited Bsc2-mNG that co-localized with a subset of LDs, the SE-only yeast contained very dim Bsc2-mNG signal that was nearly undetectable on LDs (**Fig 1D**). This suggests that TG is necessary for Bsc2-mNG LD targeting, and potentially for Bsc2-mNG protein stability.

The Bsc2 N-terminal hydrophobic regions mediate LD targeting

Proteins can target to LDs through amphipathic or hydrophobic motifs that interact with or insert into the LD PL monolayer (Bacle et al., 2017; Prévost et al., 2018; Chorlay and Thiam, 2020; Chorlay et al., 2021). To mechanistically dissect how Bsc2 targets to LDs, we examined its hydrophobicity using Phobius (Käll et al., 2004) (**Fig 2A**). The hydrophobicity plot predicted two hydrophobic regions in the N-terminal half of Bsc2, which we denote as Hydrophobic Region 1 (HR1) and Hydrophobic Region (HR2). Bsc2 also contains a predicted Low Complexity Region (LCR) directly downstream of these HRs. We hypothesized that Bsc2 targets to LDs through the action of either HR1, HR2, or both regions. To test this, we generated seven mNG-tagged fragments of Bsc2, and over-expressed them in yeast stained for LDs in LOG phase growth (**Fig 2B**). Interestingly, full length Bsc2 ($Bsc2^{FL}$) targeted both LDs and the endoplasmic reticulum (ER) when over-expressed. Similarly, a truncated fragment removing the LCR ($Bsc2^{N-HR1+HR2}$) also showed this LD and ER dual-targeting, as did a smaller fragment only containing the HR1 and HR2 regions ($Bsc2^{HR1+HR2}$), suggesting the LCR and N-terminal region ($Bsc2^{N}$) preceding HR1 are not necessary for this LD/ER localization.

Next we dissected how HR1 and HR2 influence Bsc2 localization to the ER network and LDs. A construct encoding only the N-terminal region and HR1 ($Bsc2^{N-HR1}$) localized to LDs, suggesting HR1 may be sufficient for LD targeting (**Fig 2B**). In support of this, amino acid and secondary structure analysis of HR1 indicates it forms a predicted alpha-helical fold, with several hydrophobic amino acids on one face, commonly observed in LD targeting motifs (**Fig 2A**). A smaller construct retaining HR1 without the preceding N-terminal region ($Bsc2^{HR1}$) failed to express well in yeast, suggesting the

bioRxiv preprint doi: https://doi.org/10.1101/2023.03.07.531595; this version posted March 7, 2023. The copyright holder for this preprint (which was not certified by peer review) is the author/funder. All rights reserved. No reuse allowed without permission.

initial N-terminal region may be necessary for HR1 stability. Surprisingly, a construct encoding only HR2 ($Bsc2^{HR2}$) localized primarily to the ER network surrounding the nucleus and peripheral ER (**Fig 2B**). No detectable LD localization was detected for $Bsc2^{HR2}$, indicating HR1 was necessary for detectable LD targeting. Since HR1 appeared to mediate the Bsc2 LD interaction, we generated a chimeric Bsc2 construct where we replaced HR1 with LiveDrop ($Bsc2^{LiveDrop}$), a known LD targeting module derived from the LD targeting motif of *Drosophila* GPAT4 (Wilfling et al., 2013; Wang et al., 2016). Indeed, $Bsc2^{LiveDrop}$ targeted to LDs as well as the ER network when over-expressed in yeast, and appeared similar to $Bsc2^{FL}$, suggesting LiveDrop could replace HR1 for organelle targeting (**Fig 2B**).

Bsc2 LD targeting could, in principle be due to direct insertion or interaction with the LD surface monolayer, or through binding another LD surface protein. To delineate these possibilities, we expressed yeast Bsc2-GFP in human U2-OS cells treated with oleic acid (OA) to induce LD biogenesis. Bsc2-GFP decorated the surfaces of LDs in U2-OS cells, suggesting it was able to localize to the LD surface independent of other yeast proteins (**Fig 2C**). Collectively, this supports a model where Bsc2 interacts directly with the LD surface.

Molecular dynamics simulations suggest Bsc2 HRs adopt specific conformations on TG-rich LDs

To better understand the interaction between Bsc2 and LDs, molecular dynamics (MD) simulations were conducted with $Bsc2^{N\text{-}HR1+HR2}$ (residues 1-100) interacting with a TG-rich LD (TG-only), a SE-rich LD (90:10 ratio of cholesteryl oleate (CHYO) to TG), and an ER bilayer. The structure of $Bsc2^{N\text{-}HR1+HR2}$ was first predicted with RoseTTAFold (Baek et al., 2021) and AlphaFold2 (Jumper et al., 2021), both of which predicted an alpha-helix for HR1, and a hairpin (helix-kink-helix) conformation for HR2. TOPCONS (Tsirigos et al., 2015) and TM AlphaFold (Dobson et al., 2023) also predicted a membrane-embedded topology for the hydrophobic HR2 sequence (**Fig S3M**). Although they were very similar, the RoseTTAFold structure was selected for further simulations

bioRxiv preprint doi: https://doi.org/10.1101/2023.03.07.531595; this version posted March 7, 2023. The copyright holder for this preprint (which was not certified by peer review) is the author/funder. All rights reserved. No reuse allowed without permission.

as it has been demonstrated to better predict membrane structures (Azzaz et al., 2022; Hegedűs et al., 2022).

The membrane embedded systems were set up with the HR2 hairpin inserted into each respective lipidic environment deep enough to enable the charged residues on the ends (Arg61, Asp90, Asp93, Arg100) to be surface oriented where they can interact with the charged lipid headgroups and water (**Fig 3A, Fig S3C**). The HR1 region was positioned 5 angstroms above the membrane PL to allow for membrane association between the amphipathic region and membrane packing defects (see Methods). Long timescale simulations were run on Anton2 provided by Pittsburg Supercomputing Center (Shaw et al., 2014), yielding 4.5 microseconds of simulations for the TG-only LD and ER bilayer systems. The 90:10 CHYO:TG LD system was run for 1 microsecond on EXPANSE provided by San Diego Supercomputing Center (Strande et al., 2021).

Simulations revealed clear conformational changes in Bsc2 between the LD and bilayer environments (**Fig 3A, Fig S3A-C**). In both the TG-only and 90:10 CHYO:TG LDs, HR2 orients with the predicted helix-kink-helix angle of approximately 100°, then decreases to an angle of 70°, as the kink region engages with the TG core (**Fig S3A-C**). In contrast, in the ER bilayer the helix-kink-helix region opens to an average angle of 150°, bringing the residues in the kink region closer to the PL surface (**Fig 3A**). A central driving force for this conformational change is the stabilization of polar residues Gln72, Cys75 and Ser76 near the kink of HR2. In the LDs, these residues interact with TG glycerol groups 2.0-2.5nm below the headgroup phosphates (**Fig 3B, C, Fig S3D**). In the ER bilayer, stabilization at this depth is not possible as it places the polar residues in the hydrophobic tail region of the PLs (**Fig S3E, F**). By splaying open, the kink region rises closer to the lipid head-groups, enabling polar interactions with the PL-glycerols ~1-1.2nm below the phosphate plane. Thus, HR2 obtains a kinked conformation in the LD monolayers, but a splayed open conformation in the ER bilayer.

The Bsc2 HR1 amphipathic helix embeds well in the packing defects of both the TG-rich LD and the ER bilayer (**Fig 3A**). The hydrophobic residues along the bottom of HR1

bioRxiv preprint doi: https://doi.org/10.1101/2023.03.07.531595; this version posted March 7, 2023. The copyright holder for this preprint (which was not certified by peer review) is the author/funder. All rights reserved. No reuse allowed without permission.

interact with both PL and TG acyl tails, while the charged and polar residues along the top stabilize the HR1 helix via hydrogen bonds with the PL headgroups and water. Strikingly, this is not the case for the 90:10 CHYO:TG LD. Here the HR1 helix fails to associate with the monolayer, and instead folds over on itself to maintain some degree of amphipathic interactions (**Fig 3A, right**). The reason for this discrepancy is insufficient lipid packing defects in the SE-rich LD to adequately absorb the HR1 hydrophobic moieties (**Fig 3A, Fig S3H-J**). Importantly, the amphipathic helix HR1 associates well with the TG-rich LD and ER bilayer, but fails to associate at all with the SE-rich LD.

Based on these simulations, the driving force for Bsc2 LD targeting is likely a combination of the Bsc2 HR1 and HR2 sequences working together. Due to its drastically different confirmation on TG-rich versus SE-rich (90:10 CHYO:TG) LDs, it is possible that HR1 may act as a 'sensor', detecting the numerous packing defects found on TG-rich LDs preferentially over SE-rich LDs and the ER bilayer. HR1 itself also interacts with the glycerol backbones of several TG molecules in the TG-rich LD system. Indeed, TG-rich LDs have been shown to have larger and longer-lived packing defects than the ER bilayer, with TG-LDs and ER-bilayers maintaining a packing defect constant of 27$Å^2$ and 16 $Å^2$, respectively (Kim et al., 2021; Braun and Swanson, 2022). This discrepancy is even more pronounced for the SE-rich LD, which has a more densely packed PL monolayer with very few packing defects, maintaining a defect constant of 14$Å^2$ (Braun and Swanson, 2022). Collectively, the preferential targeting of HR1 to TG-enhanced packing defects would potentially explain why the over-expressed $Bsc2^{N\text{-}HR1}$ fragment localizes to LDs, and also provides a potential molecular explanation for why Bsc2 localizes to TG-rich LDs, but appears significantly less detectable on SE-rich LDs *in vivo*.

The hydrophobic HR2 segment seems to embed in either the ER bilayer or LD monolayers. We hypothesize that in the absence of HR1, HR2 likely remains in the ER, kinetically trapped in an interfacial conformation, as observed when $Bsc2^{HR2}$ is over-expressed in yeast. However, in the presence of HR1, HR2 may fold into a more stable

bioRxiv preprint doi: https://doi.org/10.1101/2023.03.07.531595; this version posted March 7, 2023. The copyright holder for this preprint (which was not certified by peer review) is the author/funder. All rights reserved. No reuse allowed without permission.

kinked conformation once the polar residues (Gln72, Cys75, Ser76) gain access to the glycerol groups of TG molecules in the LD core (**Fig 3A**). This is supported by the depth profile of Gln72, Cys75 and Ser76 in the TG-rich LD (**Fig S3E**). Additionally, radial distribution functions (RDF) and coordination numbers $\| s \|$ verify there are strong interactions between Gln72 and Ser76 especially to TG oxygens, while the hydrophobic residues surrounding these polar residues are still stabilized by PL tails (**Fig 3B-D**). In contrast, in the ER bilayer the HR2 region opens into a more shallow interfacial conformation below the PL headgroups because of the high barrier for the polar residues to enter the PL tail region (**Fig S3F**). The relative stability of these two regions is captured in the potential of mean force (PMF) profiles (**Fig S3G**), demonstrating that Gln72 and Ser76 are most stable slightly below the PL phosphate groups, where the polar backbone and sidechain can create favorable interactions with the polar PL components. Indeed, pulling them into the lipid tail region is highly unfavorable. Considering Ser76 alone, moving from its interfacial position (~1.0 nm below the phosphate plane) to a LD kinked position (~2 nm below) would cost ~30 kJ/mol. Such high penetration barriers may explain why $Bsc2^{HR2}$ remains localized in the ER bilayer. Thus, the dynamic interplay between residues keeps the HR2 region stable within the ER bilayer, kinetically trapped in the absence of HR1, but also offers a stabilizing force in the presence of HR1, which could overcome those barriers to enable HR2 to transition to a more stable LD conformation with both polar and hydrophobic residues adopting more optimal interactions.

It is also notable that Bsc2 interacts with many TG molecules in the TG-rich LD system. HR2 coordinates with the TG-glycerol backbone, and HR1 forms several contacts with TG hydrophobic tails that intercalate into the PL monolayer (**Fig 3C,D, Fig S3H-L**). Thus, the LD core appears to require an abundance of TGs for optimal Bsc2 interactions. The proportion of conformations with a TG molecule directly interacting with a residue captures the abundance of these interactions (**Fig S3L**). The dominance of TG-interactions in the HR2 region demonstrates the sequence disposition to immerse itself within a TG-rich LD core. Additionally, the number of contacts between HR1 and TG-tails is a significant addition to its interactions with the PL-tails (**Fig S3J**).

bioRxiv preprint doi: https://doi.org/10.1101/2023.03.07.531595; this version posted March 7, 2023. The copyright holder for this preprint (which was not certified by peer review) is the author/funder. All rights reserved. No reuse allowed without permission.

Collectively, these simulations indicate that Bsc2 adopts significantly different conformational ensembles in the ER bilayer and LD environments, and that it interacts with TG molecules extensively in TG-rich LDs (**Fig 3E**). This provides a potential molecular explanation for Bsc2 preferentially targeting to TG-rich LDs.

Loss of Bsc2 alters TG levels via enhanced TG lipolysis

Because Bsc2 LD targeting appeared to require TG, and MD simulations indicated Bsc2:TG interactions, we next determined whether manipulating Bsc2 expression influenced cellular TG pools. We first examined steady-state TG and SE levels of WT and *bsc2*Δ yeast. At LOG phase, *bsc2*Δ yeast display a ~20% steady-state reduction in TG compared to WT, while SE levels are unaffected (**Fig 4A**). We reasoned this TG reduction could be the result of either enhanced lipolysis or decreased TG synthesis (or a combination of both). To dissect this, we first tested whether TG lipolysis or TG biosynthesis was altered in *bsc2*Δ yeast. Yeast contain three TG lipases: Tgl3, Tgl4, and Tgl5, of which Tgl3 performs the majority of the TG lipolysis activity in the cell (Athenstaedt and Daum, 2003, 2005). To test whether TG lipolysis was altered in *bsc2*Δ yeast, we treated WT, *bsc2*Δ, *tgl3*Δ, and *bsc2*Δ*tgl3*Δ yeast with cerulenin, which blocks *de novo* fatty acid synthesis and promotes TG lipolysis as a fatty acid source (**Fig 4B**). We then measured yeast TG levels before (T_0) and after 3hrs (T_3) of cerulenin treatment when lipolysis was active. Importantly, WT and *bsc2*Δ yeast contained similar TG levels at T_0, as we allowed yeast to grow for 24hrs into STAT phase and accumulate TG (**Fig 4C**). Notably, after 3hrs of cerulenin, WT yeast had ~60% of their TG stores remaining, whereas *bsc2*Δ only had ~20%, suggesting TG lipolysis was elevated in *bsc2*Δ yeast (**Fig 4C**). As expected, *tgl3*Δ yeast retained ~80% of their TG stores following 3hrs cerulenin (**Fig 4C**). In contrast to *bsc2*Δ yeast, *bsc2*Δ*tgl3*Δ yeast retained ~70% of their TG, behaving similar to *tgl3*Δ, suggesting the enhanced TG loss in *bsc2*Δ yeast required Tgl3. Since yeast also encode Tgl4 and Tgl5 TG lipases, we also performed cerulenin pulse experiments on WT, *bsc2*Δ, *tgl3*Δ*tgl4*Δ*tgl5*Δ, *bsc2*Δ*tgl3*Δ*tgl4*Δ*tgl5*Δ and measured TG before and after 3hrs of cerulenin (**Fig 4D**). Similarly, *tgl3*Δ*tgl4*Δ*tgl5*Δ yeast and *bsc2*Δ*tgl3*Δ*tgl4*Δ*tgl5*Δ contained near identical TG levels following 3hrs of cerulenin-

bioRxiv preprint doi: https://doi.org/10.1101/2023.03.07.531595; this version posted March 7, 2023. The copyright holder for this preprint (which was not certified by peer review) is the author/funder. All rights reserved. No reuse allowed without permission.

induced TG lipolysis. Collectively, this supports a model where *bsc2*Δ yeast exhibit enhanced TG lipolysis that is suppressed by genetic depletion of Tgl lipase activity.

Next, we determined whether Bsc2 loss alters TG biosynthesis. We utilized a yeast strain in which all of the acyltransferases that synthesize neutral lipids were deleted, with the exception of Dga1. In this strain, the DGA1 gene was placed under a galactose inducible promoter (*are1*Δ*are2*Δ*lro1*Δ^{GAL}DGA1, referred here simply as "^{GAL}DGA1") (Cartwright et al., 2015). As expected, in the absence of galactose, this yeast strain contains no neutral lipids and no LDs, and therefore staining yeast with MDH reveals no LD foci (**Fig 4E, time T=0**). In the presence of galactose in the growth media, the yeast synthesize TG via Dga1 expression and activity. We deleted *bsc2*Δ in this strain (*bsc2*Δ ^{GAL}DGA1) and compared this strain and ^{GAL}DGA1 strain's abilities to produce LDs and TG. First, we imaged LDs via MDH stain in ^{GAL}DGA1 vs *bsc2*Δ ^{GAL}DGA1 yeast at multiple timepoints after galactose induction (**Fig 4E**). Visually, there was no detectable difference in the appearance of MDH-stained LDs in *bsc2*Δ compared to WT yeasts, suggesting LD biogenesis was unperturbed by Bsc2 loss. Next, we measured whole-cell TG levels in the same strains following galactose induction of TG synthesis. We found no significant difference in TG levels between these strains over multiple time-points following GAL-induction (**Fig 4F, G**). Additionally, we detected no significant changes in free fatty acids (FFA) for either strain, although there was a slight upward trend of FFA accumulation in the *bsc2*Δ yeast after 6 hrs, potentially due to enhanced TG lipolysis (**Fig 4H**). Altogether, these results support a model where the decreased TG observed in *bsc2*Δ yeast is not due to decreased TG biosynthesis, but primarily due to enhanced Tgl3-dependent TG lipolysis.

The Bsc2 HR1 and HR2 regions are sufficient for Bsc2 function

Since the Bsc2 HR1 and HR2 regions appeared responsible for LD interactions, we next asked whether these regions were sufficient for Bsc2 function. We generated yeast with chromosomal GFP-tagged full length Bsc2 (Bsc2^{FL}-GFP) or truncated Bsc2 encoding only the N-terminal region, HR1, and HR2 (Bsc2$^{N\text{-}HR1+HR2}$-GFP). Both GFP-tagged strains localized to LDs, although Bsc2$^{N\text{-}HR1+HR2}$-GFP appeared more dimly

bioRxiv preprint doi: https://doi.org/10.1101/2023.03.07.531595; this version posted March 7, 2023. The copyright holder for this preprint (which was not certified by peer review) is the author/funder. All rights reserved. No reuse allowed without permission.

localized to LDs (**Fig 4I**). Additionally, we tested the ability of the Bsc2$^{N\text{-}HR1+HR2}$-GFP to protect against enhanced lipolysis (**Fig 4J**). As expected, initial (T_0) STAT phase TG levels for Bsc2^{FL}-GFP, Bsc2$^{N\text{-}HR1+HR2}$-GFP, and *bsc2*Δ were not significantly different (**Fig 4J**). However, after 3hrs of cerulenin-stimulated lipolysis (T_3), steady-state TG levels of yeast expressing Bsc2$^{N\text{-}HR1+HR2}$ were similar to WT yeast with Bsc2^{FL,} and significantly elevated compared to *bsc2*Δ yeast (**Fig 4J**). This suggests that the LCR region is not necessary for Bsc2 function, and that the N-HR1-HR2 region is sufficient for *in vivo* function.

Bsc2 over-expression results in TG and LD enlargement

Since Bsc2 loss appeared to enhance TG lipolysis, we next determined how Bsc2 over-expression would influence LD neutral lipids. We measured steady-state TG and SE levels of WT yeast expressing either an empty vector (EV) or over-expressed Bsc2 (Bsc2 OE) on a GPD promoter. Strikingly, we observed a more than ~4-fold increase in TG stores in Bsc2 OE yeast compared to EV controls (**Fig 5A**). In contrast, there was no effect on SE levels, suggesting Bsc2 OE selectively impacted TG pools (**Fig 5A)**. In line with this, we observed enlarged LDs in Bsc2 OE when they were imaged by thin section transmission electron microscopy (TEM) (**Fig 5B**). Quantification of TEM micrographs confirmed significantly increased LD sizes and numbers of detected LDs per thin-section of Bsc2 OE cells compared to WT (**Fig 5C, 5D**), suggesting Bsc2 OE elevated TG stores that were stored in enlarged LDs. A portion of the LDs observed in Bsc2 OE had similar area to those of EV LDs, which are likely explained by the varying expression levels of the Bsc2 OE construct. Collectively, this indicates that Bsc2 OE correlates with elevated TG levels and enlarged LDs.

A possible explanation for the TG accumulation in Bsc2 OE yeast is simply from over-expressing a hydrophobic LD surface protein, which could potentially crowd away other LD-resident proteins and perturb TG homeostasis (Kory et al., 2015). To test this possibility, we measured steady-state neutral lipid levels of yeast over-expressing Pln1 (also known as Pet10), a well characterized yeast perilipin-like protein (Gao et al., 2017), and compared these to EV and Bsc2 OE expressing yeast (**Fig 5E**). Strikingly,

bioRxiv preprint doi: https://doi.org/10.1101/2023.03.07.531595; this version posted March 7, 2023. The copyright holder for this preprint (which was not certified by peer review) is the author/funder. All rights reserved. No reuse allowed without permission.

Pln1 OE did not alter TG levels, which closely mirrored the EV control, and did not phenocopy the TG accumulation observed with Bsc2 OE (**Fig 5E**). Notably, neither of the constructs altered SE pools. This indicated that the TG and LD accumulation caused by Bsc2 OE was likely not an artifact of simply overexpressing a LD protein, and supported a model where Bsc2 OE specifically influenced LD TG levels. In support of this, Western blot analysis of Bsc2 OE and Pln1 OE expression levels revealed very similar expression levels of both proteins, suggesting they were expressing at similar high levels (**Fig 5F**). Collectively, this supports a model where Bsc2 influences LD TG pools, and that its over-expression is sufficient to induce TG accumulation.

Bsc2 loss or over-expression does not impact Tgl lipase abundance nor LD targeting

Next we investigated the mechanism by which Bsc2 influences TG lipolysis and fat accumulation. One possibility is that Bsc2 loss or over-expression may alter the total abundance or LD localization of TG lipases. To investigate this, we first performed fluorescence imaging of GFP-tagged TG lipases Tgl3, Tgl4, and Tgl5 in WT and *bsc2*Δ yeast (**Fig 6A**). Imaging revealed there were no obvious changes in Tgl lipase LD targeting in the absence of Bsc2, suggesting Tgl LD targeting was intact in *bsc2*Δ yeast. We then examined steady-state Tgl protein levels by Western blotting GFP-tagged endogenous Tgl proteins. Steady-state protein abundances of Tgl3, Tgl4, and Tgl5 were unaffected by Bsc2 loss, indicating the enhanced lipolysis observed in *bsc2*Δ yeast was not simply due to increased total lipase abundances (**Fig 6B**).

Since Bsc2 OE led to TG accumulation, we also imaged GFP-tagged Tgl proteins in WT yeast and yeast over-expressing an untagged Bsc2. As expected, yeast over-expressing Bsc2 displayed larger and more numerous LDs, but this did not alter the LD localization of any of the GFP-tagged Tgl proteins, suggesting Bsc2 OE does not inhibit their LD targeting (**Fig 6C**). Similarly, Western blotting revealed the abundances of Tgl lipases were unchanged in Bsc2 OE compared to WT, indicating that the TG accumulation in Bsc2 OE was not due to decreased lipase expression (**Fig 6D**).

bioRxiv preprint doi: https://doi.org/10.1101/2023.03.07.531595; this version posted March 7, 2023. The copyright holder for this preprint (which was not certified by peer review) is the author/funder. All rights reserved. No reuse allowed without permission.

Collectively, this indicates that changes in steady-state TG levels in *bsc2*Δ or Bsc2 OE are not due to perturbations in the abundances of TG lipases nor their LD targeting.

To determine whether Bsc2 may physically interact with Tgl lipases on the LD surface, we also conduced co-immunoprecipitation (co-IP) experiments where we over-expressed either mNG (EV-mNG) alone or Bsc2-mNG in yeast, immunoprecipitated with anti:mNG affinity resin, and examined the co-IP fractions by LC-MS/MS proteomics. Notably, numerous canonical LD proteins were significantly enriched in the Bsc2-mNG co-IP fraction, including Erg6, Hfd1, Faa1, and Eht1 (**Fig 6G**). However, we did not detect any peptides from Tgl3, Tgl4, nor Tgl5 in this experiment. While we cannot rule out that Bsc2 and Tgl lipases interact, this indicates that Bsc2 may not form functionally significant interactions with Tgl lipases.

Bsc2 and Tgl3 independently target to LD subsets

Since Bsc2 manipulation did not appear to influence Tgl3 (or any Tgl lipase) abundance or localization, we hypothesized that Bsc2 may demarcate a subset of TG-positive LDs, and interact with the TG pool there independently of Tgl lipases. If Tgl3 were to also target this Bsc2-positive LD pool, it could in principle directly compete with Bsc2 for TG access on the monolayer surface. In this model, Bsc2 may function as a negative regulator of TG lipolysis through stochastic competition for TG. If so, then depletion of Bsc2 would result in elevated lipolysis, and Bsc2 over-expression would promote TG accumulation. In support of this model, MD simulations indicated that Bsc2 strongly interacted with TG in model LDs (**Fig 3**).

To test this model, we directly compared Bsc2 and Tgl3 LD localizations in yeast co-expressing chromosomally tagged Bsc2-GFP and Tgl3-mRuby. Prior to cerulenin treatment (T_0), we observed LDs with detectable levels of both Bsc2-GFP and Tgl3-mRuby (**Fig 6E, yellow arrows**), as well as LDs exhibiting only detectable Bsc2-GFP (**Fig 6E, green arrows**) or Tgl3-mRuby alone (**Fig 6E, red arrows**). This indicated that Bsc2 and Tgl3 can occupy the same LD, but also distinct LD subsets within a cell, suggesting they target to LDs independently of one another.

bioRxiv preprint doi: https://doi.org/10.1101/2023.03.07.531595; this version posted March 7, 2023. The copyright holder for this preprint (which was not certified by peer review) is the author/funder. All rights reserved. No reuse allowed without permission.

Next, we imaged these same dual-labeled yeast following 3hrs (T_3) of cerulenin treatment to induce lipolysis (**Fig 6E**). We then quantified LDs for Bsc2-GFP and Tgl3-mRuby signal above background, and generated signal correlation graphs (**Fig 6F**). Notably, at T_0 there is a heterogenous mix of Bsc2-GFP and Tgl3-mRuby signals on LDs, with some LDs displaying abundant Tgl3-mRuby signal but low Bsc2-GFP signal (Tgl3>Bsc2, upper-left region of chart, red circle), LDs with significant levels of both Bsc2-GFP and Tgl3-mRuby signals (Tgl3~Bsc2, center to upper-right region of chart), and LDs with high Bsc2-GFP but low Tgl3-mRuby signal (Bsc2>Tgl3, lower right region of chart). In line with this, the Pearson correlation was relatively low, r=0.3701. This variation of Bsc2-to-Tgl3 signal supports a model where these two proteins independently target to LDs.

Following 3hrs of cerulenin treatment, the Bsc2-GFP/Tgl3-mRuby LD signal distribution changed. LDs now displayed a more linear positive correlation pattern, with Bsc2-GFP signal correlating with Tgl3-mRuby signal (i.e., Tgl3~Bsc2), and a Pearson correlation of r=0.8774 (**Fig 6F, red circle**). Collectively, this supports a model where LDs with detectable Tgl3, but low or undetectable Bsc2, may be depleted or altered during TG lipolysis, whereas LDs with more abundant Bsc2-GFP are retained following 3hrs cerulenin-induced TG lipolysis.

Bsc2 loss alters LD accumulation in yeast stationary phase

As yeast transition into STAT phase, they enter slow growth and shunt excess lipids into TG for long-term storage. Since Bsc2 loss elevated TG lipolysis, we queried whether *bsc2*Δ yeast would display differences in LD abundances as they transitioned into long-term STAT phase. We quantified the number of LDs per yeast cell for WT and *bsc2*Δ yeast initially cultured in 2% glucose media and allowed to grow continually in this media for six days (defined as gradual glucose restriction, GGR). At the start of the experiment (T=0 days), when cells were in early STAT phase, *bsc2*Δ yeast exhibited more MDH-stained LDs compared to WT (**Fig 7A, B**). However, following six days of GGR, *bsc2*Δ yeast displayed significantly fewer LDs per cell than WT yeast (**Fig 7A, B**).

bioRxiv preprint doi: https://doi.org/10.1101/2023.03.07.531595; this version posted March 7, 2023. The copyright holder for this preprint (which was not certified by peer review) is the author/funder. All rights reserved. No reuse allowed without permission.

This supports a model where Bsc2 depletion causes elevated TG lipolysis, which over time would gradually deplete LD stores in yeast subsisting in long-term low-nutrient conditions. Collectively, we propose a model in which Bsc2 labels a subset of TG-containing LDs and marks them for preservation from lipolysis, which could in principle be utilized as a lipid source in stationary phase subsistence (**Fig 7C**).

Discussion:

Emerging work indicates that LDs can be classified into distinct subpopulations within single cells, and such LD subsets are differentiated by unique proteomes, morphologies, or spatial distributions (Thiam and Beller, 2017; Eisenberg-Bord et al., 2018; Teixeira et al., 2018; Schott et al., 2019; Ugrankar et al., 2019). A key knowledge gap is how distinct proteomes confer specific functions to LD subpopulations. Here, we demonstrate that Bsc2 is a yeast protein with amphipathic and hydrophobic regions that enriches on a subpopulation of LDs and acts as negative regulator of TG lipolysis. We also find that Bsc2 LD targeting requires TG, and MD simulations reveal that Bsc2 hydrophobic regions adopt specific conformations on TG-rich LDs and engage in extensive interactions with TG. Loss of Bsc2 reduces steady state TG levels at LOG growth phase (but does not alter SE pools), and we find this is due to enhanced lipolysis and not by decreased TG synthesis. Bsc2 over-expression accumulates whole-cell TG and enlarged LDs, a phenotype not replicated by overexpressing another hydrophobic LD coat protein Pln1/Pet10. We hypothesize this is due to a Bsc2-dependent block in lipolysis, though this does not exclude other changes such as elevated TG synthesis or LD biogenesis as contributing factors. We also find that yeast lacking Bsc2 display altered LD mobilization in late-phase STAT phase. This may indicate that in the absence of Bsc2, lipolysis in STAT phase is dysregulated and LDs are differentially mobilized, supporting a model where Bsc2 helps maintain a LD subset for longer-term subsistence.

A pervasive question in LD biology is how proteins target to LDs. One factor that clearly influences both LD protein targeting and stability is the presence of neutral lipids in LDs (Grillitsch et al., 2011; Schmidt et al., 2013; Klein et al., 2016; Gao et al., 2017; Prévost

bioRxiv preprint doi: https://doi.org/10.1101/2023.03.07.531595; this version posted March 7, 2023. The copyright holder for this preprint (which was not certified by peer review) is the author/funder. All rights reserved. No reuse allowed without permission.

et al., 2018; Chorlay and Thiam, 2020; Rogers et al., 2022). Our Bsc2 structure-function analysis indicate that both HR1 and HR2 contribute to organelle targeting. In line with this, MD simulations indicate that HR1 and HR2 undergo significant conformation changes in response to different lipid environments. On LDs, HR2 adopts a more compact helix-kink-helix conformation and interacts with TG, in contrast to a more "splayed open" conformation in the ER bilayer. HR1 also interacts extensively with TG and PLs on the LD surface, but disengages entirely from the SE-rich LD surface. This indicates that both HR1 and HR2 may enable Bsc2 to anchor on LDs, but HR1 may act as a LD "compositional sensor", preferentially engaging TG-rich LDs and potentially explaining why Bsc2 is detected on only LD subsets that may have more accessible TG *in vivo*. In the absence of TG, Bsc2 may adopt a less favorable conformation and be targeted for degradation, although further studies are needed for confirmation. This may explain why Bsc2 LD targeting is significantly less detectable in SE-only yeast.

How does Bsc2 regulate TG lipolysis? We show that Bsc2 loss or over-expression does not alter Tgl lipase LD targeting nor protein abundance, and co-IP mass spectrometry analysis indicated that Bsc2 does not detectably interact with Tgl3. This collectively suggests that Bsc2 is likely not a strong interactor with Tgl lipases, and therefore does not likely regulate lipolysis through strong direct enzyme interactions. An alternative hypothesis is that Bsc2 competes with Tgl3 for TG-binding on the LD surface by occupying lipid packing defects, effectively altering TG substrate availability and prohibiting Tgl lipases from mobilizing TG.

Previous visual screens have identified a number of yeast proteins that target LD subpopulations and aid in the formation and maintenance of specific LD subsets. The most studied examples are the isoforms Ldo16 and Ldo45, which demarcate a specific pool of LDs formed near the yeast nucleus-vacuole junction, and are determinants of the targeting of other LD proteins, such as Pdr16, to these spatially distinct LDs (Eisenberg-Bord et al., 2018; Teixeira et al., 2018; Ren et al., 2014). During their investigation into Ldo45/Ldo16 function, Eisenberg-Bord et al also identified Bsc2 as a marker of the Pdr16-enriched LD subset (Eisenberg-Bord et al., 2018). Our study now

bioRxiv preprint doi: https://doi.org/10.1101/2023.03.07.531595; this version posted March 7, 2023. The copyright holder for this preprint (which was not certified by peer review) is the author/funder. All rights reserved. No reuse allowed without permission.

characterizes Bsc2 as a regulator of TG lipolysis, as well as provides a working model for how it localizes to a subset of TG-rich LDs. In the future, we hope to further reveal the function of this Bsc2-positive LD subset in yeast physiology and metabolic adaptation.

Acknowledgements:

The authors would like to thank members of the Henne and Swanson labs for conceptual help on this manuscript. We also thank Jonathan Friedman, Joel Goodman, and Daniela Nicastro for conceptual assistance. We would also like to thank Joel Goodman for providing W303 yeast strains for this study. Finally, we would like to thank the UT Southwestern proteomics, electron microscopy, and live cell imaging core facilities for their aid with data collection and analysis.. W.M.H, N.O.S. and E.G.R. are supported by grants from the Welch Foundation (I-1873), the NIH NIGMS (GM119768), NIDDK (DK126887), the Ara Parseghian Medical Research Fund, and the UT Southwestern Endowed Scholars Program. J.M.J.S. and R.J.B are supported by NIH NIGMS (R35GM143117) and are grateful for computational support from ANTON 2 at the Pittsburgh Supercomputing Center (MCB210016P), EXPANSE at the San Diego Supercomputing Center through the ACCESS program (allocation MCB200018) supported by NSF (grants #2138259, #2138286, #2138307, #2137603, and #2138296), as well as the Center for High Performance Computing at the University of Utah.

Methods:

Yeast growth conditions

The WT parental strain used for all experiments and cloning in this study was BY4741 (MATa *his3*Δ1 *leu2*Δ0 *met15*Δ0 *ura3*Δ0). W303-1A (MATa leu2-3, 112 trp1-1 can1-100 ura3-1 ade2-1 his3-11,14) yeast strain was used as the parental strain for imaging of yeast with different neutral lipid-containing backgrounds (Fig 1E) and for galactose induced TG synthesis experiments (Fig 4E-H). Synthetic-complete (SC) growth media was used for culturing yeast cells in all experiments, except for experiments where uracil was excluded to retain pBP73G or pRS316 plasmids. For all experiments (unless noted below), a colony of yeast was inoculated from a YPD (yeast extract peptone

bioRxiv preprint doi: https://doi.org/10.1101/2023.03.07.531595; this version posted March 7, 2023. The copyright holder for this preprint (which was not certified by peer review) is the author/funder. All rights reserved. No reuse allowed without permission.

dextrose) plate into SCD (SC dextrose/glucose) media and allowed to grow for ~ 24hr in a 30°C incubator with shaking at 210 rpm. These cultures were diluted to OD_{600} = 0.001 in SCD media containing 2% glucose (wt/vol), grown overnight in a 30˚C incubator shaking at 210 rpm, and collected at mid-log phase (~OD_{600} = 0.6) the next day. For cerulenin experiments, yeast were cut back to OD_{600} = 0.1 in SCD media from an overnight culture and grown for 24hr, 30˚C, 210 RPM. 50 OD_{600} units were collected from the 24hr culture as pre-lipolysis sample (Time 0hrs, "T_0"). The remainder of the 24hr culture was cut back to OD_{600} = 0.5 in fresh SCD media containing 10µg/µL Cerulenin (Cat# C2389; Sigma-Aldrich) final concentration and allowed to incubate for 3hrs before harvesting 50 OD_{600} units as a post-lipolysis sample (Time 3hrs, "T_3"). Aliquots were then washed in MiliQ water, pelleted, and then processed for lipid extraction and TLC. Culturing of yeast for cerulenin imaging experiments (Fig 5E) was done as detailed above, except a small aliquot was removed from 24hr culture as T_0 and ~25 OD_{600} was removed at T_3 from SCD plus Cerulenin cultures. All samples were concentrated down to 1mL in their respective media, and LDs stained for 5 min with MDH (SM1000a; Abcepta) at a final concentration of 0.1 mM before imaging. For induction of TG synthesis, ^{GAL}DGA1 yeast strains were first cultured in 0.2% dextrose SCD media, overnight. Cells were then pelleted, washed in MiliQ water, and resuspended in 2% raffinose SCR media (2% raffinose substituted for dextrose in SCD) at OD_{600} = 0.5 and cultured for 24hrs. Following 24hr incubation, 50 OD_{600} units were removed as Time 0 ("T_0") sample for lipid extraction and TLC. The remainder of the yeast were pelleted, washed in MiliQ water, then cut back to OD_{600} = 2 in SCG media (2% galactose substituted for dextrose in SCD), and incubated for 22hrs. 50 OD_{600} unit aliquots were removed at 2, 4, 6, and 22hrs incubation, washed in Mili-Q water, then pelleted and processed for lipid extraction and TLC. For imaging of induced LDs, ^{GAL}DGA1 yeast strains were cultured same as above, except 1mL aliquots were taken from SCG cultures at indicated time points and incubated for 5 min with MDH at a final concentration of 0.1 mM to visualize LDs. For gradual glucose restriction LD imaging experiments, yeast were cultured from a plate overnight in SCD media. 1mL of overnight culture was taken for Day 0, stained with MDH and LDs were imaged. The remainder of the culture was cut back to OD_{600} = 0.1 in fresh SCD media and incubated

bioRxiv preprint doi: https://doi.org/10.1101/2023.03.07.531595; this version posted March 7, 2023. The copyright holder for this preprint (which was not certified by peer review) is the author/funder. All rights reserved. No reuse allowed without permission.

for 6 days, with 1mL aliquots taken each day and LDs imaged after staining with MDH. For immunoprecipitation and proteomics, cells were cultured from plates into SCD-URA (without uracil) overnight. Then, yeast were cut back to OD_{600} = 0.1 into same drop-out media, then incubated for 24hrs (under general growth conditions described above) until they reached stationary phase. After 24hrs, 250 OD_{600} units were collected for each sample, pelleted at 4000 RPM for 5 min, washed in Mili-Q water then pelleted again. Final yeast pellets were then subjected for protein extraction and immunoprecipitation.

Molecular Dynamics Simulations

Structure prediction: TOPCONS (Tsirigos et al., 2015) and TmAlphaFold (Dobson et al., 2023) were used to predict the membrane-embedded regions of Bsc2. The protein structure prediction tools RoseTTAFold (Baek et al., 2021) and AlphaFold2 (Jumper et al., 2021) were then used to model the structure of $Bsc2^{N\text{-}HR1+HR2}$ (amino acids 1-100). The resulting output poses from both resources agreed on the placement and alignment of all helices within the protein. This included HR1 in a single amphipathic helical structure and HR2 in a helix-kink-helix structure. The final structure was taken from RoseTTAFold, using no pairing or templates. Notably, the 5 top-scoring structures from RoseTTAFold had quite similar alignment. The output for TOPCONS transmembrane topology and the selected final structure are in Figures S3M and S3C, respectively.

Simulations: The CHARMM36 force field (Campomanes et al., 2021), (Klauda et al., 2010) was used in all simulations. The bilayer system was created in the CHARMM-GUI membrane builder (Jo et al., 2008) with a ratio of 88:37:10 ratio of 3-palmitoyl-2-oleoyl-D-glycero-1-phosphatidylcholine (POPC), 2,3-dioleoyl-D-glycero-1-phosphatidylethanolamine (DOPE), and phosphatidylinositol (SAPI), respectively. This corresponds to 135 PLs per leaflet (270 PLs total per system). The LD systems had the same membrane compositions for their respective monolayer leaflets and included an 8 nm thick neutral lipid core composed of a 90:10 CHYO:TG ratio for the SE-rich LD and a pure-TG core for the TG-rich LD. These LD structures were taken from the last frame of 8 µs long simulations conducted in our previous work, which importantly had already obtained the properly equilibrated distributions (Braun and Swanson, 2022). The

bioRxiv preprint doi: https://doi.org/10.1101/2023.03.07.531595; this version posted March 7, 2023. The copyright holder for this preprint (which was not certified by peer review) is the author/funder. All rights reserved. No reuse allowed without permission.

membrane systems were embedded in 5nm of water and 0.15M NaCl on top and bottom to account for proper hydration and physiological conditions. To insert the Bsc2 structure into the membrane systems, in-house MDAnalysis (Gowers et al., 2016) scripting was used, placing HR2 into the bilayer and LD monolayers and HR1 0.5 nm above the membrane. Overlapping PLs and neutral lipids were removed and the systems were minimized for 5000 steps before being re-equilibrated for 10 ns using NVT conditions and 100 ns using NPT conditions. For the bilayer and TG-LD systems, long-timescale simulations lasting 4.5 μs were conducted using the Anton2 supercomputer provided by Pittsburg Supercomputing Center (Shaw et al., 2014), while the 90:10 CHYO:TG system was run for 1 μs on the EXPANSE supercomputer provided by San Diego Supercomputing Center (Strande et al., 2021). The simulations were conducted using a 2.4 fs timestep in the Anton2 simulations, and a 2 fs timestep in the EXPANSE simulation. The temperatures were all set to 310 K, using Nose-Hoover thermostat (Nosé, 1984),(Hoover, 1985) and a temperature coupling time constant of 1 ps. The particle mesh Ewald (PME) algorithm (Essmann et al., 1995) was used to calculate the long-range electrostatic interactions with a cutoff of 1.0 nm. Lennard–Jones pair interactions were cutoff at 12 Å with a force-switching function between 8 and 12 Å, and pressure was maintained semi-isotropically using the Parrinello-Rahman barostat (Parrinello and Rahman, 1981). The pressure was set to 1.0 bar, with a compressibility of, $4 \times 10^{-5}\, bar^{-1}$, and a coupling constant of 5.0 ps. The hydrogen bonds were constrained with the LINCS algorithm (Hess, 2008). We calculated the coordination numbers, RDFs, and protein positions using MDAnalysis, and in-house Python scripting, and Gromacs tools (Abraham et al., 2015), and the images were rendered using Visual Molecular Dynamics (VMD) (Humphrey et al., 1996).

Metadynamics: Potentials of mean force (PMFs) for single amino acids permeating through a bilayer were conducted using Well-Tempered Metadynamics (Barducci et al., 2008) biasing the *z*-component connecting the center of mass of the membrane and the center of mass of the amino acid. The bilayers used for the metadynamics simulations were created from same initial systems described above. The system was hydrated 5 nm of water surrounding each side with 0.15 M NaCl, and the respective amino acid

bioRxiv preprint doi: https://doi.org/10.1101/2023.03.07.531595; this version posted March 7, 2023. The copyright holder for this preprint (which was not certified by peer review) is the author/funder. All rights reserved. No reuse allowed without permission.

was placed 2 nm above the membrane surface. The amino acids included in our simulations were Phe, Gln, Leu, Ser. The amino acids were neutralized by patching with the NH2 (CT2) group at the C-terminus, and an acetyl (ACE) at the N-terminus. Four replicas of each amino acid system were run for 500 ns each. The final PMF was obtained by averaging the PMFs obtained from the four simulations. The Gaussian function was deposited every 2 ps with a height of 0.05 kJ/mol and the bias factor was set to 15. Simulations were conducted in the canonical ensemble (NVT) at a temperature of 310K, using the Gromacs version 2019.4 (Abraham et al., 2015) patched with PLUMED version 2.5.3 (Tribello et al., 2014).

Lipid extraction and TLC

For lipid extraction, 50 OD_{600} units of cells were collected for each sample, and pellet wet weights were normalized and recorded prior to extraction. Lipid extraction was performed using a modified Folch method (Folch et al., 1957). Briefly, cell pellets were resuspended in Milli-Q water with 0.5-mm glass beads (Cat # G8772-500G; Milipore Sigma) and lysed by three 1-min cycles on a MiniBeadBeater. Chloroform and methanol were added to the lysate to achieve a 2:1:1 chloroform:methanol:water ratio. Samples were vortexed, centrifuged to separate the organic solvent and aqueous phases, and the organic solvent phase was collected. Extraction was repeated a total of three times. The organic solvent phases were combined and washed twice with 1 ml 1.0 M KCl. Prior to TLC, lipid samples were dried under a stream of argon gas and resuspended in 1:1 chloroform:methanol to a final concentration corresponding to 4 µl of solvent per 1 mg cell pellet wet weight. Isolated lipids were spotted onto heated glass-backed silica gel 60 plates (1057210001; Millipore Sigma), and neutral lipids were separated in a mobile phase of 80:20:1 hexane:diethyl ether:glacial acetic acid. TLC bands were visualized by spraying dried plates with cupric acetate in 8% phosphoric acid and baking at 145°C for an hour.

TLC quantification

Stained TLC plates were scanned and then processed for quantification using Fiji (ImageJ). Each plate was spotted with a neutral lipid reference standard mixture (Cat #

bioRxiv preprint doi: https://doi.org/10.1101/2023.03.07.531595; this version posted March 7, 2023. The copyright holder for this preprint (which was not certified by peer review) is the author/funder. All rights reserved. No reuse allowed without permission.

18-5C; Nu-Chek Prep). The standard was prepared in chloroform to a final concentration of 10 mg/ml and diluted to 1µg/µL before loading onto plate. The neutral lipid standard was used to create a standard curve in which the x-axis displayed the calculated lipid mass in micrograms, and the y-axis displayed the band intensity estimated by using Fiji.

LD number and area quantification

For Fig 5B TEM images, LDs were counted by hand using the Fiji multipoint tool. The area of these same LDs was determined by tracing the perimeter of each by hand using the Fiji freehand line tool. Each LD was selected as an ROI, then the area quantified using the "Measure" tool in Fiji and reported in μm^2. For fluorescence images in Fig 7A, LD number per cell was quantified by counting MDH-stained LDs, by hand, using the Fiji multipoint tool.

Fluorescent signal quantification of Bsc2 and Tgl3 imaging under cerulenin treatment

In Fig 6F, fluorescent signals for Bsc2-GFP and Tgl3-mRuby foci were quantified from confocal maximal projections from Fig 6E imaging using Fiji. To summarize, for each image, the midplane z-section of the DAPI channel (MDH-stained LDs) was converted to grayscale, then random LDs were selected using the oval selection tool. Each of these LDs were marked as individual ROIs, along with a random area with no fluorescent signal selected as background, then all were saved to the ROI manager. Next, the maximal projections for the DAPI, RFP, and GFP channels were merged into one image, and the previously selected LD ROIs were overlaid on to image. The fluorescent signal for each channel, represented as Raw Integrated Density, was then measured for each ROI. These values were then subtracted from the background ROI integrated density for each channel to obtain a Bsc2-GFP and Tgl3-mRuby signal value for each ROI. Then, for both GFP and mRuby channels, each ROI signal measurement was divided by the ROI with highest Raw Integrated Density to obtain a ratio (Raw Integrated Density / Max Integrated Density). For each ROI, said ratio for Bsc2-GFP signal and Tgl3-mRuby signal were plotted against each other for "No Cerulenin" and

bioRxiv preprint doi: https://doi.org/10.1101/2023.03.07.531595; this version posted March 7, 2023. The copyright holder for this preprint (which was not certified by peer review) is the author/funder. All rights reserved. No reuse allowed without permission.

"3hr Cerulenin" conditions. Pearson's correlation coefficient (r) was calculated for both graphs.

Statistical analysis

Graphpad Prism 8 software was used to perform all statistical analyses, with graphs indicating the mean + standard deviation. Two-tailed, unpaired t tests were performed with Welch's correction. Where indicated, ordinary one-way ANOVA tests were performed, with Tukey's multiple comparisons test applied. For both t tests and ANOVA, ns, $P \geq 0.05$; *, $P < 0.05$; **, $P < 0.01$; ***, $P < 0.001$; ****, $P < 0.0001$.

Conventional TEM

Yeast cells were grown in the desired conditions and processed in the University of Texas Southwestern Electron Microscopy Core Facility using a adapted protocol from Wright (Wright, 2000). In brief, cells were fixed in potassium permanganate, dehydrated, and stained in uranyl acetate and embedded in Spurr Resin. Specimen blocks were polymerized at 60°C overnight and sectioned at 70 nm with a diamond knife (Diatome) on a Leica Ultracut UCT 6 ultramicrotome (Leica Microsystems). Sections were poststained with 2% uranyl acetate in water and lead citrate. Sections were placed on copper grids (Thermo Fisher Scientific). Images were acquired on a Tecnai G2 spirit TEM (FEI) equipped with a LaB6 source at 120 kV by using a Gatan Ultrascan charge-coupled device camera.

Whole cell protein extraction and sample preparation

Whole cell protein extracts were isolated from 25 OD_{600} units of cells. Pellet wet weights were normalized prior to freezing at −20°C. Frozen cell pellets were incubated with 20% trichloroacetic acid (TCA) for 30 min on ice with occasional mixing using a vortex. Precipitated proteins were pelleted in a 4°C centrifuge at 16,000 g for 5 min. After removing the supernatant, the pellet was washed three times with cold 100% acetone followed by brief sonication. After the washes, the protein pellets were dried in an RT speed vac for 15 min to remove residual acetone. Dried protein pellets were neutralized with 1.5M Tris-HCl pH 8.8, then resuspended directly in 250µL of 1X Laemelli sample

bioRxiv preprint doi: https://doi.org/10.1101/2023.03.07.531595; this version posted March 7, 2023. The copyright holder for this preprint (which was not certified by peer review) is the author/funder. All rights reserved. No reuse allowed without permission.

buffer (Laemmli, 1970). Samples were briefly sonicated and boiled at 95˚C for 5 min. Fig 5F protein samples (Bsc2-mNG OE and Pln1-mNG OE) were extracted as described above, except following neutralization, protein pellets were resuspended in 250µL resuspension buffer (50mM Tris pH 6.8, 1mM EDTA, 1% SDS; 6M Urea, 1X Halt Protease and Phosphatase Inhibitor Cocktail [78441; Thermo Fisher Scientific], and 1% beta-mercaptoethanol). These samples were sonicated briefly, but not subjected to heating/boiling to prevent aggregation of these hydrophobic droplet proteins. 2X Laemelli sample buffer was added to these samples immediately prior to gel loading.

Immunoblot analysis

Following protein extraction, samples were pelleted at 16,000 g for 3 min to remove insoluble debris. Equal volumes of each sample were then subjected to SDS-PAGE and western blot analysis. Proteins were separated on a precast Mini-PROTEAN® TGX™ 10% SDS-PAGE gel (4561034; BioRad) and then transferred to a 0.45 µm nitrocellulose membrane in Towbin SDS transfer buffer (25 mM Tris, 192 mM glycine, 20% methanol, and 0.05% SDS; pH 8.2) using a Criterion tank blotter with plate electrodes (1704070; BioRad) set to 70V constant, for 1hr. Immediately after transfer, membranes were stained with PonceauS, imaged on a ChemiDoc™ Touch Gel Imager (1708370; BioRad) and cut using a clean razor blade. Membranes were blocked with 5% milk dissolved in Tris-buffered saline +Tween (TBS-T) buffer, and primary antibodies were allowed to bind overnight at 4°C. Primary antibodies used for determining protein expression are as follows: GFP (ab290; 1:5,000 dilution; Abcam), GAPDH (ab9485; 1:2,500 dilution; Abcam), mNeonGreen (Cat# 32f6; 1:1,000 dilution; ChromoTek). Immunoblots were developed by binding HRP-conjugated anti-rabbit IgG (ab6721;1:5,000; Abcam) or anti-mouse IgG (ab6728; 1:1,000; Abcam) secondary antibodies to the membrane for 1 h in the presence of 5% milk followed by four washes in TBS-T and developing with ECL substrate (1705061; BioRad). Blot signal was captured using the same BioRad ChemiDoc™ Touch Gel Imager, as noted above. Protein expression levels were quantified by measuring band intensity using ImageJ and normalizing these values to wildtype to generate an abundance value relative to control.

bioRxiv preprint doi: https://doi.org/10.1101/2023.03.07.531595; this version posted March 7, 2023. The copyright holder for this preprint (which was not certified by peer review) is the author/funder. All rights reserved. No reuse allowed without permission.

Whole cell protein extraction for immunoprecipitation

Yeast were collected and prepared as described above. The samples were subjected to a modified cold glass bead cell lysis and protein extraction protocol (DeCaprio and Kohl, 2020). In brief, cells were washed in cold tris-buffered saline and pelleted at 2000 g for 5 min at 4˚C. Yeast pellets were resuspended in ice-cold lysis buffer plus protease inhibitors (50mM Tris-HCl pH 7.5, 120mM KCl, 5mM EDTA, 0.1% Nonidet P-40 Substitute, 10% Glycerol, 1mM DTT, 1mM PMSF, and 1X Halt Protease and Phosphatase Inhibitor Cocktail [78441; Thermo Fisher Scientific]), transferred to a 2 mL screw-cap microcentrifuge tube (Cat # 02-681-343; Fisher Scientific) containing glass beads (Cat # G8772-500G; Milipore Sigma), and lysed 3 times in a MiniBeadBeater for 90 sec each at 4˚C. In between bead beating, samples were chilled in an ice bath for 2 min. Samples were then pelleted at 1000 g at 4˚C for 30 sec. Supernatants were transferred to a 1.5 mL microcentrifuge tube, and beads in screw-cap tubes were washed once again in the same lysis buffer plus protease inhibitors and pelleted like above. Supernatants of screw-cap tubes were transferred to same 1.5 mL tube as above, and were cleared of insoluble debris, twice at 16000 g for 10 min at 4˚C. A final clearance spin of lysates was done at 20000 g for 30 min at 4˚C. Protein concentrations were then quantified using the Pierce™ BCA Protein Assay Kit (Cat # 23227; Thermo Fisher Scientific) in a 96-well plate format (Cat # 353072; Corning). Sample absorbances were measured at 562 nm using a VersaMax Microplate Reader and SoftMax Pro Software. Absorbances were converted to protein concentration using a bovine serum albumin standard curve.

Immunoprecipitation (IP)

For immunoprecipitation, an mNeonGreen-Trap Agarose Kit (ntak-20; Chromotek) to pull down Bsc2-mNeonGreen (mNG) fusion protein was used, according to manufacturer's protocol. To begin, for each sample 25µL of agarose beads containing an anti-mNG nanobody were washed in 500µL of ice cold dilution buffer (10mM Tris-HCl pH 7.5, 150mM NaCl, 0.5mM EDTA, and 0.018% sodium azide), centrifuged down at 2500 g for 5 min at 4˚C, and buffer removed. 4000 µg of protein lysate from cold

bioRxiv preprint doi: https://doi.org/10.1101/2023.03.07.531595; this version posted March 7, 2023. The copyright holder for this preprint (which was not certified by peer review) is the author/funder. All rights reserved. No reuse allowed without permission.

glass bead lysis for each sample was centrifuged at 16000 g, 5 min, at 4˚C. Then, lysates were incubated with the washed mNG beads and rotated end over end for 1 hr at 4˚C. Samples were then spun down at 2500 g for 5 min at 4˚C and supernatants removed. Beads were then washed three times in 500µL wash buffer (10 mM Tris/Cl pH 7.5, 150 mM NaCl, 0.05 % Nonidet™ P40 Substitute, 0.5 mM EDTA, and 0.018 % sodium azide) and centrifuged like above, in between each wash. After final wash and spin, supernatant was removed, beads were transferred to a fresh 1.5 mL tube. 2X Laemmli sample buffer was added to beads, and samples were boiled for 5 min at 95˚C

LC-MS/MS proteomics

Following boiling step, IP samples were centrifuged at 2500 g, for 2 min at 4˚C to pellet beads. The entirety of each supernatant was loaded onto a 10% mini-protean TGX gel (4561033; Bio-Rad). Samples were subjected to electrophoresis at 90 V constant until the dye front was ~10 cm into the gel. The gel was subsequently removed from the casing and stained with Coomassie reagent (0.5 Coomassie G-250, 50% methanol, 10%
acetic acid) for 10 min on an RT rocker. The gel was then rinsed three times in sterile Mili-Q water to gently destain. Once the gel was sufficiently destained, 10-cm gel bands were excised from each lane, taking care to exclude the stacking gel and dye front. Gel bands were further cut into 1-mm squares and placed into sterile microcentrifuge tubes. Samples were digested overnight with trypsin (Pierce) following reduction and alkylation with DTT and iodoacetamide (Sigma-Aldrich). The samples then underwent solid-phase extraction cleanup with an Oasis HLB plate (Waters), and the resulting samples were injected onto an Orbitrap Fusion Lumos mass spectrometer coupled to an Ultimate 3000 RSLC-Nano liquid chromatography system. Samples were injected onto a 75 µm i.d., 75-cm long EasySpray column (Thermo Fisher Scientific) and eluted with a gradient from 0 to 28% buffer B over 90 min. The buffer contained 2% (vol/vol) acetonitrile and 0.1% formic acid in water, and buffer B contained 80% (vol/vol) acetonitrile, 10% (vol/vol) trifluoroethanol, and 0.1% formic acid in water. The mass spectrometer operated in positive ion mode with a source voltage of 1.5–2.0 kV and an ion transfer tube temperature of 275°C. MS scans were acquired at 120,000 resolution in the

bioRxiv preprint doi: https://doi.org/10.1101/2023.03.07.531595; this version posted March 7, 2023. The copyright holder for this preprint (which was not certified by peer review) is the author/funder. All rights reserved. No reuse allowed without permission.

Orbitrap, and up to 10 MS/MS spectra were obtained in the ion trap for each full spectrum acquired using higher-energy collisional dissociation for ions with charges 2–7. Dynamic exclusion was set for 25 s after an ion was selected for fragmentation. RawMS data files were analyzed using Proteome Discoverer v 2.4 (Thermo Fisher Scientific), with peptide identification performed using Sequest HT searching against the *Saccharomyces cerevisiae* protein database from UniProt. Fragment and precursor tolerances of 10 ppm and 0.6 dalton were specified, and three missed cleavages were allowed. Carbamidomethylation of Cys was set as a fixed modification, with oxidation of Met set as a variable modification. The false-discovery rate cutoff was 1% for all peptides.

Cell culture

U2-OS cells were cultured in DMEM (D5796; Sigma) supplemented with 10% Cosmic Calf Serum (SH30087.04; Hyclone), 1% penicillin streptomycin solution (30-002-Cl; Corning), and 25mM HEPES (H0887;Sigma). The cells were passaged when they reached 80–90% con- fluence with 0.25% trypsin-EDTA (25-053-Cl; Corning). To promote LD biogenesis, cells were incubated with 600 μM of OA conjugated with 100 μM of FA-free BSA (A8806; Sigma-Aldrich) for 16 hours.

Cloning and transient transfection

Full length Bsc2-EGFP was generated after PCR amplification of full length Bsc2 from a yeast pBP73G Bsc2 untagged overexpression plasmid and cloning into pEGFP-N2 (XhoI/BamHI). pEGFP-N2 alone, served as a negative control. The plasmids were transfected into U2-OS cells using Lipofectamine 3000 Transfection Reagent (L3000001; Invitrogen) and Opti-MEM (31985-070; Gibco) for 48 h before experiments.

IF staining

Cells were fixed with 4% PFA solution in PBS for 15 min at RT. For IF staining, fixed cells were washed with PBS, permeabilized with 0.2% NP-40 in PBS at RT for 3 min, and blocked in IF buffer (PBS containing 3% BSA, 0.1% NP-40, and 0.02% sodium azide) for 45 min. The cells were then incubated with primary antibody in IF buffer for 1

bioRxiv preprint doi: https://doi.org/10.1101/2023.03.07.531595; this version posted March 7, 2023. The copyright holder for this preprint (which was not certified by peer review) is the author/funder. All rights reserved. No reuse allowed without permission.

h, washed thrice with PBS, incubated with secondary antibody in IF buffer for 30 min, and given two washes with PBS. Cells were then incubated with MDH AutoDOT (SM1000a; 1:1,000 dilution; Abcepta) for 15 min, washed thrice with PBS, and then stored in PBS at 4˚C before imaging. The primary antibody used was mouse anti-Hsp90B1 (AMAb91019; 1:100 dilution; Sigma-Aldrich). The secondary antibody used was donkey anti-mouse Rhodamine Red-X (715-295-151; 1:1,000 dilution; Jackson Laboratories). LDs were visualized by staining the cells with AutoDOT.

Fluorescence microscopy

For confocal microscopy, yeast cells were grown as described above and collected by centrifugation at 4,000 rpm for 5 min. Where indicated, cells were incubated for 5 min with MDH (SM1000a; Abcepta) at a final concentration of 0.1 mM to visualize LDs. Before imaging, yeast cells were washed with 1 ml of Mili-Q water and resuspended in 50-100µL of Mili-Q water. Mammalian cells were imaged in 8-well Nunc™ Lab-Tek™ II chambered coverglass (Cat #154409; Thermo Scientific). All images were taken as single slices at approximately mid-plane using a Zeiss LSM880 inverted laser scanning confocal microscope equipped with Zen software. Images were taken with a 63x oil objective NA = 1.4 or 40x oil objective NA = 1.4 at RT, unless noted otherwise. Approximately seven Z-sections of each image were taken for yeast, and four for mammalian cells. The merged images were maximum intensity z-projections, generated by Fiji. For epifluorescence microscopy, cells were grown, stained, and collected as described above. Imaging was performed on an EVOS FL Cell Imaging System at RT.

Yeast strain generation and plasmid construction

A modified version of the lithium acetate method was used for the generation of all yeast knock outs and knock ins. Briefly, yeast were diluted from a ~24h culture to an OD_{600} = 0.001 in YPD media and allowed to grow 16-20h, overnight, until they reached OD600 = 0.6. For each transformation, the entire culture was pelleted (50mL), washed with sterile Mili-Q water, washed with 0.1 M lithium acetate, pelleted and resuspended in 1mL 0.1M lithium acetate. 100µL this yeast-lithium acetate suspension was added to ~1mL of transformation solution (40% polyethylene glycol in 0.1 M lithium acetate, 0.25

bioRxiv preprint doi: https://doi.org/10.1101/2023.03.07.531595; this version posted March 7, 2023. The copyright holder for this preprint (which was not certified by peer review) is the author/funder. All rights reserved. No reuse allowed without permission.

µg/µl single-stranded carrier DNA [D9156; Sigma-Aldrich]) supplemented with 5-10µg of PCR product. Transformations were vortexed and incubated at 30˚C for 45 min, then 42˚C for 30 min. Cells were then pelleted at 2000 g, 2 min and gently washed with sterile Mili-Q water, then pelleted again. For antibiotic marker transformations, yeast were then resuspended in 2mL fresh YPD media and allowed to recover overnight, 30˚C, 225 RPM. The following day, cells were pelleted and plated onto YPD plates containing antibiotic and incubated at 30˚C, 2-3 d. For auxotrophic marker transformations, yeast were plated onto SC dropout plates same day (immediately after Mili-Q washing step) and incubated at 30˚C, 2-3 d. Plasmids were generated for this study using Gibson Assembly following the manufacturer's protocol (E2611; NEB). All pBP73-G vectors were cut with XbaI and XhoI. For yeast plasmid transformations, cells were grown in YPD media, overnight until saturation. 1 mL of overnight culture was pelleted at 12000 RPM, 2 min at RT. Pellets were then washed in 0.1M Lithium Acetate and centrifuged again, like above. Yeast cells were then resuspended in ~300 µL transformation solution (40% polyethylene glycol in 0.1 M lithium acetate, 0.25 µg/µl single-stranded carrier DNA [D9156; Sigma-Aldrich]) with 1µg of plasmid DNA, vortexed briefly, and incubated at RT for 1hr. Transformations were then gently mixed, DMSO added to a final concentration of 10%, and heat shocked at 42˚C, 10 min. Samples were then put on ice for 2 min, then entire reaction was plated onto SCD plates lacking uracil, and incubated at 30˚C for 2-3 days.

Proteomics quantification

Proteomics quantification and analysis were performed using Excel. All samples were analyzed in triplicate. To adjust for total protein differences between samples, the sum of all spectral counts within each sample was taken and divided by the average of the spectral count sums in the empty vector soluble mNG (EV-mNG) samples. This ensured differences observed in the proteomics data are not due to unequal "loading" into the MS. Next, only proteins with detectable spectral counts in all 3 replicates of the Bsc2-mNG IP samples were considered for analyses, regardless of whether they were present in the EV-mNG IP replicates. From this list proteins, those with undetectable spectral counts in the EV-mNG IP replicates had their spectral counts changed from "0"

bioRxiv preprint doi: https://doi.org/10.1101/2023.03.07.531595; this version posted March 7, 2023. The copyright holder for this preprint (which was not certified by peer review) is the author/funder. All rights reserved. No reuse allowed without permission.

to "1" to aid in quantifications for statistical analysis. To generate a high-confidence list of Bsc2 interacting proteins, the average spectral counts of each protein from the Bsc2-mNG IPs were divided by the corresponding average spectral counts from the EV-mNG IP samples. Therefore, proteins more abundant in the Bsc2-mNG IP samples would produce a ratio >0. To generate volcano plots in GraphPad Prism, $\log_2$ values were calculated for the ratio of average protein expression in EV-mNG and Bsc2-mNG (i.e., $\log_2$[protein A in Bsc2-mNG/protein A in EV-mNG]). Then, the p-value for significance of the abundance for each protein in EV-mNG and Bsc2-mNG replicate samples was calculated via t test. Finally, the $-\log_{10}$ of these p-values was calculated and plotted against the above log2 values in volcano plot form. Significance cut-off on the y-axis was the -log10 of P = 0.05, or 1.3.

Cartoon development

All cartoons created with BioRender.com or Microsoft Powerpoint. For Fig 2A, the hydrophobicity plot was generated using data collected from Phobius open access hydrophobicity predictor (Käll et al., 2004) and the helical wheel generated using HeliQuest (Gautier et al., 2008).

<u>Figure Legends:</u>

Figure 1. Bsc2 enriches on a TG-containing LD subpopulation at logarithmic phase. (A) Logarithmic (LOG) and stationary (STAT) phase imaging of yeast dual-tagged for Bsc2-GFP, Erg6-mRuby. Yellow arrows indicate Bsc2-enriched LDs and white arrows indicate LDs where Bsc2 is undetectable or absent. **(B)** Quantification of percentage of Bsc2-positive ($Bsc2^+$) LDs out of total Erg6-mRuby LDs, per cell, at LOG and STAT phase. For both LOG and STAT samples, n = 50 cells. **(C)** Bsc2-GFP expressing yeast stained with LD dye MDH and imaged at LOG phase growth. Yellow arrows are Bsc2-positive LDs, white arrows denote Bsc2-negative LDs. **(D)** Imaging of Bsc2-mNeonGreen (Bsc2-mNG) yeast in different neutral lipid-containing backgrounds with MDH-stained LDs at LOG phase. TG = Triglyceride, SE = Sterol Ester. Far left column represents non-contrast adjusted images for Bsc2-mNG. Statistics represent Unpaired t test with Welch's correction. ***, P < 0.001. Scale bars, 5µm.

bioRxiv preprint doi: https://doi.org/10.1101/2023.03.07.531595; this version posted March 7, 2023. The copyright holder for this preprint (which was not certified by peer review) is the author/funder. All rights reserved. No reuse allowed without permission.

Figure 2. Hydrophobic Region 1 (HR1) of Bsc2 is responsible for LD-targeting.

(A) Hydrophobicity plot generated by Phobius online transmembrane topology and signal peptide predictor (top), paired with a schematic of Bsc2 protein architecture (middle), and a helical wheel of the Bsc2 amphipathic segment in HR1 (bottom). HR1 = Hydrophobic Region 1, HR2 = Hydrophobic Region 2. **(B)** Log phase imaging of yeast over-expressing various Bsc2-mNG truncations with LDs stained with MDH. Yellow arrows indicate LD-targeting. LCR = Low Complexity Region. **(C)** Imaging of U2-OS cells transiently overexpressing either empty vector (EV-EGFP) or Bsc2, both tagged with EGFP (Bsc2-EGFP) and treated with oleic acid (OA), overnight to induce LD formation. Cells were coIF stained with α-EGFP (green), α-HSP90B1 (ER, red), and LDs stained with MDH (blue) and imaged with confocal microscope. Inset shows Bsc2-LD targeting. Mammalian scale bar, 10 µm. Yeast scale bar, 5µm.

Figure 3: Molecular dynamics simulations indicate Bsc2 adopts a unique conformational ensemble on TG-rich LDs

(**A**) In the modeled ER bilayer (left), the HR2 sequence opens to allow polar residues in the kink to evade the unfavorable phospholipid (PL) tail region. In the TG-rich LD (middle) polar residues (purple and orange) are stabilized by TG glycerol groups in the LD core. In the SE-rich LD (right), HR2 retains a kinked conformation with polar residues stabilized by Cholesteryl oleate (CHYO) oxygens in the LD core. Notably, the amphipathic HR1 sequence fails to LD associate due to significantly decreased packing defects. (**B**) Radial distribution functions (RDF) of GLN, CYS, and SER in the HR2 interacting with TG glycerol oxygens. (**C**) Cross section of the LD monolayer highlights interactions between GLN72 (purple), SER76 (yellow) and TG oxygens (inset). (**D**) The coordination number between residue heavy atoms and different sections of the TG molecules verifies that most interactions are with the glycerol (GL) group. (**E**) Schematic of modeled $Bsc2^{N\text{-}HR1\text{-}HR2}$ adopting conformations in the ER bilayer, TG-rich LD, and SE-rich LD as in Panel A.

Figure 4. Bsc2 deletion results in enhanced Tgl3 lipase-dependent TG lipolysis

bioRxiv preprint doi: https://doi.org/10.1101/2023.03.07.531595; this version posted March 7, 2023. The copyright holder for this preprint (which was not certified by peer review) is the author/funder. All rights reserved. No reuse allowed without permission.

(A) Log phase, whole cell TG (left graph) and SE (right graph) levels of wildtype (WT) and *bsc2*Δ yeast, measured by TLC. Experiments conducted in triplicate. Statistical analysis is Unpaired t test with Welch's correction. **(B)** Graphical schematic of cerulenin lipolysis assay for yeast. **(C, left panel)** TLC quantification of STAT phase, pre-lipolysis (T_0) TG levels of WT, *bsc2*Δ, *tgl3*Δ, and *bsc2*Δ*tgl3*Δ. **(C, right panel)** Rate of lipolysis determined via TLC after addition of 10µg/µL cerulenin (T_3) for these same strains. Quantification represents percentage of starting TG remaining (pre-cerulenin TG levels set to 100% for each strain) after 3hrs of cerulenin-stimulated lipolysis. Experiments conducted in triplicate. Statistical analyses are ordinary one-way ANOVA. **(D, left panel)** TLC quantification of STAT phase, pre-lipolysis TG levels of WT, *bsc2*Δ, *tgl3*Δ*tgl4*Δ *tgl5*Δ, and *bsc2*Δ*tgl3*Δ*tgl4*Δ *tgl5*Δ. **(D, right panel)** Rate of lipolysis determined via TLC after addition of 10µg/µL cerulenin for these same strains. Quantification represents percentage of starting TG remaining (pre-cerulenin TG levels set to 100% for each strain) after 3hrs of cerulenin-stimulated lipolysis. Experiments conducted in triplicate. Statistical analyses are ordinary one-way ANOVA. **(E)** Time-lapse imaging of galactose-induced LD formation in WT ^{GAL}DGA1 and *bsc2*Δ ^{GAL}DGA1 yeast stained with MDH. Scale bar 2µm. **(F)** Representative TLC plate of galactose-induced TG production in WT ^{GAL}DGA1 and *bsc2*Δ ^{GAL}DGA1 yeast strains. FFA = Free Fatty Acids, ERG = Ergosterol, DG = Diacylglyceride. **(G)** TLC quantification of TG levels after galactose-induced TG production time-course in WT ^{GAL}DGA1 and *bsc2*Δ ^{GAL}DGA1. Representative of three independent experiments. Statistical analyses are multiple unpaired t tests with Welch's correction. **(H)** TLC quantification of FFA levels after galactose-induced TG production time-course in WT ^{GAL}DGA1 and *bsc2*Δ ^{GAL}DGA1. Representative of three independent experiments. Statistical analyses are multiple unpaired t tests with Welch's correction. **(I)** LOG phase imaging of endogenous WT full-length Bsc2-GFP (Bsc2^{FL}-GFP) and truncated Bsc2 with GFP inserted after HR2 (Bsc2$^{N\text{-}HR1+HR2}$-GFP), with MDH stained LDs. Scale bar 5µm. **(J, left panel)** TLC quantification of STAT phase, pre-lipolysis TG levels of Bsc2^{FL}-GFP, *bsc2*Δ, and Bsc2$^{N\text{-}HR1+HR2}$-GFP. **(J, right panel)** Rate of lipolysis determined via TLC after addition of 10µg/µL cerulenin for these same strains. Quantification represents percentage of starting TG remaining (pre-cerulenin TG levels set to 100% for each strain) after 3hrs of

bioRxiv preprint doi: https://doi.org/10.1101/2023.03.07.531595; this version posted March 7, 2023. The copyright holder for this preprint (which was not certified by peer review) is the author/funder. All rights reserved. No reuse allowed without permission.

cerulenin-stimulated lipolysis. Experiments conducted in triplicate. Statistical analyses are ordinary one-way ANOVA. *, P < 0.05; **, P < 0.01; ***, P < 0.001; ****, P < 0.0001.

Figure 5. Overexpression of Bsc2 significantly elevates TG levels, LD number and LD size. (A) Steady state, LOG phase, TG (left panel) and SE (right panel) levels in empty vector plus soluble GFP (EV) and Bsc2-mNeonGreen overexpressing (Bsc2 OE) yeast as quantified by TLC. Data were compiled from three independent experiments. **(B)** Thin-section TEM micrographs of LOG phase EV and Bsc2 OE yeast. LD = Lipid Droplet, N = Nucleus, V = Vacuole. **(C)** LD number quantification from Fig 5B micrographs. n = 44 cells for EV and n = 18 cells for Bsc2 OE. **(D)** LD area quantification from Fig 5B micrographs. n = 98 LDs for EV and n = 115 LDs for Bsc2 OE. **(E)** Steady state TG (left panel) and SE (right panel) levels at LOG for EV, Bsc2 OE, and Pln1 overexpressing (Pln1 OE) yeast. Experiments were performed in triplicate. **(F)** Protein expression of Bsc2-mNeonGreen and Pln1-mNeonGreen overexpressing constructs used in Fig 5E. Membranes blotted with anti-mNeonGreen antibody and Ponceau S stain served as loading control for total protein. Scale bars, 0.5 µm. Statistics for Fig 5A, C, and D were unpaired t test with Welch's correction. Statistics for Fig 5E was ordinary one-way ANOVA. *, P < 0.05; ***, P < 0.001; ****, P < 0.0001.

Figure 6. Bsc2 does not alter TG lipase LD-targeting or protein abundance, but modulates lipolysis on the LD. (A, C) Fluorescence imaging of GFP-tagged TG lipases in either WT and *bsc2*Δ (A) or EV and untagged Bsc2 OE yeast (C). LDs were stained with MDH. **(B, D)** Protein expression levels of GFP-tagged TG lipases in WT and *bsc2*Δ (B) and EV and Bsc2 OE (D). Red asterisks indicated GFP-tagged lipases. Data is normalized to WT or EV, respectively, and represents three independent experiments. **(E)** Fluorescence imaging of Bsc2-GFP and Tgl3-mRuby dual-tagged yeast, with MDH stained LDs before (T_0) and 3hrs after cerulenin-stimulated lipolysis (T_3). Green arrows indicate Bsc2-enriched LDs, red arrows indicate Tgl3-enriched LDs, and yellow arrows indicate LDs targeted with both Bsc2 and Tgl3. Second from left column represents non-contrast adjusted images for Tgl3-mRuby. **(F)** Scatterplot of

bioRxiv preprint doi: https://doi.org/10.1101/2023.03.07.531595; this version posted March 7, 2023. The copyright holder for this preprint (which was not certified by peer review) is the author/funder. All rights reserved. No reuse allowed without permission.

Bsc2-GFP fluorescence signal intensity versus Tgl3-mRuby signal intensity for random LDs before (T_0) and after 3hrs cerulenin treatment (T_3) with Pearson's correlation coefficient (r) displayed. Data corresponding to images in Fig 6E. Red circles indicate Tgl3-enriched/Bsc2-deenriched LDs. n = 120 LDs for each condition, quantified from 87 cells for T_0 and 105 cells for T_3. **(G)** Volcano plot showing negative Log_{10} P value (-Log_{10}) and Log_2 abundance changes for Bsc2 IP interactors versus EV control, obtained via mass spec analysis. Red text at select data points indicates LD proteins found to directly interact with Bsc2. Red dotted line indicates significance cut-off for protein hits. Data were collected from three independent experiments. Statistical analyses are multiple unpaired t tests. Scale bars are 5µm. ns, ≥ 0.05.

Figure 7. Bsc2 influences LD maintenance during late starvation conditions. **(A)** Imaging of MDH-stained WT and *bsc2*Δ yeast LDs, before (Day 0) and after (Day 6) exposure to late STAT phase, also known as Gradual Glucose Restriction (GGR). Blue circles indicate cell borders. **(B)** Quantification of LD number per cell at Day 0 and Day 6 of exposure to GGR, from images in Fig 7A. n = 150 cells for both WT and *bsc2*Δ, each. **(C)** Cartoon model of Bsc2 negative regulation of Tgl3-dependent TG lipolysis via competition for TG substrate binding or direct interaction (WT LD, left). In the absence of Bsc2, TG is more accessible to Tgl3 lipase (*bsc2*Δ LD, right). Statistics are unpaired t test with Welch's correction. Scale bars, 5µm. **, P < 0.01; ****, P < 0.0001.

<u>Figure Supplements:</u>

Figure Supplement 3: MD analysis of Bsc2 HR1 and HR2 conformations. (**A**) The angle of HR2 over time in simulation. (**B**) Schematic of HR2 helix-kink-helix region. The coordinates of the angle were taken between the endpoints (residues 61 and 100) and the kink (residue 78). The predicted/initial angle was 100 degrees. (**C**) The predicted structure of Bsc2 N+HR1+HR2 through RoseTTAFold. (**D**) Average depths from of residues 60-99 (sidechains) below the PL phosphate plane in the TG-rich LD and ER bilayer. Focusing on the polar residues, the average depth of the residue's COM is significantly deeper in the TG-LD (**E**) than in the (**F**) ER bilayer. (**G**) The free energy profile for membrane permeation shows the stability of GLN and SER ~1nm below the

bioRxiv preprint doi: https://doi.org/10.1101/2023.03.07.531595; this version posted March 7, 2023. The copyright holder for this preprint (which was not certified by peer review) is the author/funder. All rights reserved. No reuse allowed without permission.

phosphate plane just under the headgroups (dark green regions) and unfavorable penalty for pulling them ~2 nm below the plane into the PL tail region (light green region). (**H**) HR1 sequence interacting with the bilayer (top) and TG-LD (bottom). (**I**) In the ER bilayer, these contacts are all PL-tail interactions. (**J**) In the TG-LD system, there is a combination of PL-tail and TG defects interactions. (**K**) In the SE-rich 90:10 CHYO:TG LD, the interactions rarely occur as there are too few packing defects. (**L**) The probability of each residue interacting with a TG molecule through the entire simulation. The HR2 sequence is almost in constant contact with TG molecules. (**M**) TOPCONS prediction of transmembrane segments (grey and white bars), which correspond to the HR2 helices.

References:

Abraham, M.J., T. Murtola, R. Schulz, S. Páll, J.C. Smith, B. Hess, and E. Lindahl. 2015. GROMACS: High performance molecular simulations through multi-level parallelism from laptops to supercomputers. *SoftwareX*. 1–2:19–25. doi:10.1016/j.softx.2015.06.001.

Athenstaedt, K., and G. Daum. 2003. YMR313c/TGL3 Encodes a Novel Triacylglycerol Lipase Located in Lipid Particles of Saccharomyces cerevisiae. *J. Biol. Chem.* 278:23317–23323. doi:10.1074/jbc.M302577200.

Athenstaedt, K., and G. Daum. 2005. Tgl4p and Tgl5p, Two Triacylglycerol Lipases of the Yeast Saccharomyces cerevisiae Are Localized to Lipid Particles. *J. Biol. Chem.* 280:37301–37309. doi:10.1074/jbc.M507261200.

Athenstaedt, K., D. Zweytick, A. Jandrositz, S.D. Kohlwein, and G. Daum. 1999. Identification and Characterization of Major Lipid Particle Proteins of the Yeast *Saccharomyces cerevisiae*. *J. Bacteriol.* 181:6441–6448. doi:10.1128/JB.181.20.6441-6448.1999.

Azzaz, F., N. Yahi, H. Chahinian, and J. Fantini. 2022. The Epigenetic Dimension of Protein Structure Is an Intrinsic Weakness of the AlphaFold Program. *Biomolecules*. 12:1527. doi:10.3390/biom12101527.

Bacle, A., R. Gautier, C.L. Jackson, P.F.J. Fuchs, and S. Vanni. 2017. Interdigitation between Triglycerides and Lipids Modulates Surface Properties of Lipid Droplets. *Biophys. J.* 112:1417–1430. doi:10.1016/j.bpj.2017.02.032.

Baek, M., F. DiMaio, I. Anishchenko, J. Dauparas, S. Ovchinnikov, G.R. Lee, J. Wang, Q. Cong, L.N. Kinch, R.D. Schaeffer, C. Millán, H. Park, C. Adams, C.R. Glassman, A. DeGiovanni, J.H. Pereira, A.V. Rodrigues, A.A. van Dijk, A.C. Ebrecht, D.J. Opperman, T. Sagmeister, C.

bioRxiv preprint doi: https://doi.org/10.1101/2023.03.07.531595; this version posted March 7, 2023. The copyright holder for this preprint (which was not certified by peer review) is the author/funder. All rights reserved. No reuse allowed without permission.

Buhlheller, T. Pavkov-Keller, M.K. Rathinaswamy, U. Dalwadi, C.K. Yip, J.E. Burke, K.C. Garcia, N.V. Grishin, P.D. Adams, R.J. Read, and D. Baker. 2021. Accurate prediction of protein structures and interactions using a three-track neural network. *Science*. 373:871–876. doi:10.1126/science.abj8754.

Barducci, A., G. Bussi, and M. Parrinello. 2008. Well-Tempered Metadynamics: A Smoothly Converging and Tunable Free-Energy Method. *Phys. Rev. Lett.* 100:020603. doi:10.1103/PhysRevLett.100.020603.

Bersuker, K., C.W.H. Peterson, M. To, S.J. Sahl, V. Savikhin, E.A. Grossman, D.K. Nomura, and J.A. Olzmann. 2018. A Proximity Labeling Strategy Provides Insights into the Composition and Dynamics of Lipid Droplet Proteomes. *Dev. Cell*. 44:97-112.e7. doi:10.1016/j.devcel.2017.11.020.

Braun, R.J., and J.M.J. Swanson. 2022. Capturing the Liquid-Crystalline Phase Transformation: Implications for Protein Targeting to Sterol Ester-Rich Lipid Droplets. *Membranes*. 12:949. doi:10.3390/membranes12100949.

Caillon, L., V. Nieto, P. Gehan, M. Omrane, N. Rodriguez, L. Monticelli, and A.R. Thiam. 2020. Triacylglycerols sequester monotopic membrane proteins to lipid droplets. *Nat. Commun.* 11:3944. doi:10.1038/s41467-020-17585-8.

Campomanes, P., J. Prabhu, V. Zoni, and S. Vanni. 2021. Recharging your fats: CHARMM36 parameters for neutral lipids triacylglycerol and diacylglycerol. *Biophys. Rep.* 1:None. doi:10.1016/j.bpr.2021.100034.

Cartwright, B.R., D.D. Binns, C.L. Hilton, S. Han, Q. Gao, and J.M. Goodman. 2015. Seipin performs dissectible functions in promoting lipid droplet biogenesis and regulating droplet morphology. *Mol. Biol. Cell*. 26:726–739. doi:10.1091/mbc.E14-08-1303.

Chorlay, A., L. Forêt, and A.R. Thiam. 2021. Origin of gradients in lipid density and surface tension between connected lipid droplet and bilayer. *Biophys. J.* 120:5491–5503. doi:10.1016/j.bpj.2021.11.022.

Chorlay, A., and A.R. Thiam. 2020. Neutral lipids regulate amphipathic helix affinity for model lipid droplets. *J. Cell Biol.* 219:e201907099. doi:10.1083/jcb.201907099.

Currie, E., X. Guo, R. Christiano, C. Chitraju, N. Kory, K. Harrison, J. Haas, T.C. Walther, and R.V. Farese. 2014. High confidence proteomic analysis of yeast LDs identifies additional droplet proteins and reveals connections to dolichol synthesis and sterol acetylation. *J. Lipid Res.* 55:1465–1477. doi:10.1194/jlr.M050229.

DeCaprio, J., and T.O. Kohl. 2020. Lysing Yeast Cells with Glass Beads for Immunoprecipitation. *Cold Spring Harb. Protoc.* 2020:pdb.prot098590. doi:10.1101/pdb.prot098590.

bioRxiv preprint doi: https://doi.org/10.1101/2023.03.07.531595; this version posted March 7, 2023. The copyright holder for this preprint (which was not certified by peer review) is the author/funder. All rights reserved. No reuse allowed without permission.

Dhiman, R., S. Caesar, A.R. Thiam, and B. Schrul. 2020. Mechanisms of protein targeting to lipid droplets: A unified cell biological and biophysical perspective. *Semin. Cell Dev. Biol.* 108:4–13. doi:10.1016/j.semcdb.2020.03.004.

Dobson, L., L.I. Szekeres, C. Gerdán, T. Langó, A. Zeke, and G.E. Tusnády. 2023. TmAlphaFold database: membrane localization and evaluation of AlphaFold2 predicted alpha-helical transmembrane protein structures. *Nucleic Acids Res.* 51:D517–D522. doi:10.1093/nar/gkac928.

Duncan, R.E., M. Ahmadian, K. Jaworski, E. Sarkadi-Nagy, and H.S. Sul. 2007. Regulation of Lipolysis in Adipocytes. *Annu. Rev. Nutr.* 27:79–101. doi:10.1146/annurev.nutr.27.061406.093734.

Eisenberg-Bord, M., M. Mari, U. Weill, E. Rosenfeld-Gur, O. Moldavski, I.G. Castro, K.G. Soni, N. Harpaz, T.P. Levine, A.H. Futerman, F. Reggiori, V.A. Bankaitis, M. Schuldiner, and M. Bohnert. 2018. Identification of seipin-linked factors that act as determinants of a lipid droplet subpopulation. *J. Cell Biol.* 217:269–282. doi:10.1083/jcb.201704122.

Essmann, U., L. Perera, M.L. Berkowitz, T. Darden, H. Lee, and L.G. Pedersen. 1995. A smooth particle mesh Ewald method. *J. Chem. Phys.* 103:8577–8593. doi:10.1063/1.470117.

Gao, Q., D.D. Binns, L.N. Kinch, N.V. Grishin, N. Ortiz, X. Chen, and J.M. Goodman. 2017. Pet10p is a yeast perilipin that stabilizes lipid droplets and promotes their assembly. *J. Cell Biol.* 216:3199–3217. doi:10.1083/jcb.201610013.

Gautier, R., D. Douguet, B. Antonny, and G. Drin. 2008. HELIQUEST: a web server to screen sequences with specific α-helical properties. *Bioinformatics*. 24:2101–2102. doi:10.1093/bioinformatics/btn392.

Gluchowski, N.L., M. Becuwe, T.C. Walther, and R.V. Farese. 2017. Lipid droplets and liver disease: from basic biology to clinical implications. *Nat. Rev. Gastroenterol. Hepatol.* 14:343–355. doi:10.1038/nrgastro.2017.32.

Gowers, R., M. Linke, J. Barnoud, T. Reddy, M. Melo, S. Seyler, J. Domański, D. Dotson, S. Buchoux, I. Kenney, and O. Beckstein. 2016. MDAnalysis: A Python Package for the Rapid Analysis of Molecular Dynamics Simulations. Austin, Texas. 98–105.

Grillitsch, K., M. Connerth, H. Köfeler, T.N. Arrey, B. Rietschel, B. Wagner, M. Karas, and G. Daum. 2011. Lipid particles/droplets of the yeast Saccharomyces cerevisiae revisited: Lipidome meets Proteome. *Biochim. Biophys. Acta BBA - Mol. Cell Biol. Lipids*. 1811:1165–1176. doi:10.1016/j.bbalip.2011.07.015.

Hariri, H., S. Rogers, R. Ugrankar, Y.L. Liu, J.R. Feathers, and W.M. Henne. 2018. Lipid droplet biogenesis is spatially coordinated at ER –vacuole contacts under nutritional stress. *EMBO Rep.* 19:57–72. doi:10.15252/embr.201744815.

bioRxiv preprint doi: https://doi.org/10.1101/2023.03.07.531595; this version posted March 7, 2023. The copyright holder for this preprint (which was not certified by peer review) is the author/funder. All rights reserved. No reuse allowed without permission.

Hegedűs, T., M. Geisler, G.L. Lukács, and B. Farkas. 2022. Ins and outs of AlphaFold2 transmembrane protein structure predictions. *Cell. Mol. Life Sci.* 79:73. doi:10.1007/s00018-021-04112-1.

Heier, C., and R.P. Kühnlein. 2018. Triacylglycerol Metabolism in *Drosophila melanogaster*. *Genetics*. 210:1163–1184. doi:10.1534/genetics.118.301583.

Hess, B. 2008. P-LINCS: A Parallel Linear Constraint Solver for Molecular Simulation. *J. Chem. Theory Comput.* 4:116–122. doi:10.1021/ct700200b.

Hoover, W.G. 1985. Canonical dynamics: Equilibrium phase-space distributions. *Phys. Rev. A*. 31:1695–1697. doi:10.1103/PhysRevA.31.1695.

Humphrey, W., A. Dalke, and K. Schulten. 1996. VMD: visual molecular dynamics. *J. Mol. Graph*. 14:33–38, 27–28. doi:10.1016/0263-7855(96)00018-5.

Jo, S., T. Kim, V.G. Iyer, and W. Im. 2008. CHARMM-GUI: A web-based graphical user interface for CHARMM. *J. Comput. Chem.* 29:1859–1865. doi:10.1002/jcc.20945.

Jumper, J., R. Evans, A. Pritzel, T. Green, M. Figurnov, O. Ronneberger, K. Tunyasuvunakool, R. Bates, A. Žídek, A. Potapenko, A. Bridgland, C. Meyer, S.A.A. Kohl, A.J. Ballard, A. Cowie, B. Romera-Paredes, S. Nikolov, R. Jain, J. Adler, T. Back, S. Petersen, D. Reiman, E. Clancy, M. Zielinski, M. Steinegger, M. Pacholska, T. Berghammer, S. Bodenstein, D. Silver, O. Vinyals, A.W. Senior, K. Kavukcuoglu, P. Kohli, and D. Hassabis. 2021. Highly accurate protein structure prediction with AlphaFold. *Nature*. 596:583–589. doi:10.1038/s41586-021-03819-2.

Käll, L., A. Krogh, and E.L.L. Sonnhammer. 2004. A Combined Transmembrane Topology and Signal Peptide Prediction Method. *J. Mol. Biol.* 338:1027–1036. doi:10.1016/j.jmb.2004.03.016.

Kim, S., M.I. Oh, and J.M.J. Swanson. 2021. Stressed Lipid Droplets: How Neutral Lipids Relieve Surface Tension and Membrane Expansion Drives Protein Association. *J. Phys. Chem. B*. 125:5572–5586. doi:10.1021/acs.jpcb.1c01795.

Klauda, J.B., R.M. Venable, J.A. Freites, J.W. O'Connor, D.J. Tobias, C. Mondragon-Ramirez, I. Vorobyov, A.D. MacKerell, and R.W. Pastor. 2010. Update of the CHARMM All-Atom Additive Force Field for Lipids: Validation on Six Lipid Types. *J. Phys. Chem. B*. 114:7830–7843. doi:10.1021/jp101759q.

Klein, I., L. Klug, C. Schmidt, M. Zandl, M. Korber, G. Daum, and K. Athenstaedt. 2016. Regulation of the yeast triacylglycerol lipases Tgl4p and Tgl5p by the presence/absence of nonpolar lipids. *Mol. Biol. Cell*. 27:2014–2024. doi:10.1091/mbc.E15-09-0633.

bioRxiv preprint doi: https://doi.org/10.1101/2023.03.07.531595; this version posted March 7, 2023. The copyright holder for this preprint (which was not certified by peer review) is the author/funder. All rights reserved. No reuse allowed without permission.

Koch, B., C. Schmidt, B. Ploier, and G. Daum. 2014. Modifications of the C terminus Affect Functionality and Stability of Yeast Triacylglycerol Lipase Tgl3p. *J. Biol. Chem.* 289:19306–19316. doi:10.1074/jbc.M114.556944.

Kory, N., A.-R. Thiam, R.V. Farese, and T.C. Walther. 2015. Protein Crowding Is a Determinant of Lipid Droplet Protein Composition. *Dev. Cell*. 34:351–363. doi:10.1016/j.devcel.2015.06.007.

Kurat, C.F., K. Natter, J. Petschnigg, H. Wolinski, K. Scheuringer, H. Scholz, R. Zimmermann, R. Leber, R. Zechner, and S.D. Kohlwein. 2006. Obese Yeast: Triglyceride Lipolysis Is Functionally Conserved from Mammals to Yeast. *J. Biol. Chem.* 281:491–500. doi:10.1074/jbc.M508414200.

Laemmli, U.K. 1970. Cleavage of Structural Proteins during the Assembly of the Head of Bacteriophage T4. *Nature*. 227:680–685. doi:10.1038/227680a0.

Li, Z., K. Thiel, P.J. Thul, M. Beller, R.P. Kühnlein, and M.A. Welte. 2012. Lipid Droplets Control the Maternal Histone Supply of Drosophila Embryos. *Curr. Biol.* 22:2104–2113. doi:10.1016/j.cub.2012.09.018.

Müllner, H., D. Zweytick, R. Leber, F. Turnowsky, and G. Daum. 2004. Targeting of proteins involved in sterol biosynthesis to lipid particles of the yeast Saccharomyces cerevisiae. *Biochim. Biophys. Acta BBA - Biomembr.* 1663:9–13. doi:10.1016/j.bbamem.2004.03.001.

Nosé, S. 1984. A unified formulation of the constant temperature molecular dynamics methods. *J. Chem. Phys.* 81:511–519. doi:10.1063/1.447334.

Parrinello, M., and A. Rahman. 1981. Polymorphic transitions in single crystals: A new molecular dynamics method. *J. Appl. Phys.* 52:7182–7190. doi:10.1063/1.328693.

Prévost, C., M.E. Sharp, N. Kory, Q. Lin, G.A. Voth, R.V. Farese, and T.C. Walther. 2018. Mechanism and Determinants of Amphipathic Helix-Containing Protein Targeting to Lipid Droplets. *Dev. Cell*. 44:73-86.e4. doi:10.1016/j.devcel.2017.12.011.

Ren, J., C. Pei-Chen Lin, M.C. Pathak, B.R.S. Temple, A.H. Nile, C.J. Mousley, M.C. Duncan, D.M. Eckert, T.J. Leiker, P.T. Ivanova, D.S. Myers, R.C. Murphy, H.A. Brown, J. Verdaasdonk, K.S. Bloom, E.A. Ortlund, A.M. Neiman, and V.A. Bankaitis. 2014. A phosphatidylinositol transfer protein integrates phosphoinositide signaling with lipid droplet metabolism to regulate a developmental program of nutrient stress–induced membrane biogenesis. *Mol. Biol. Cell*. 25:712–727. doi:10.1091/mbc.e13-11-0634.

Rogers, S., L. Gui, A. Kovalenko, V. Zoni, M. Carpentier, K. Ramji, K. Ben Mbarek, A. Bacle, P. Fuchs, P. Campomanes, E. Reetz, N.O. Speer, E. Reynolds, A.R. Thiam, S. Vanni, D. Nicastro, and W.M. Henne. 2022. Triglyceride lipolysis triggers liquid crystalline phases

bioRxiv preprint doi: https://doi.org/10.1101/2023.03.07.531595; this version posted March 7, 2023. The copyright holder for this preprint (which was not certified by peer review) is the author/funder. All rights reserved. No reuse allowed without permission.

in lipid droplets and alters the LD proteome. *J. Cell Biol.* 221:e202205053. doi:10.1083/jcb.202205053.

Sandager, L., M.H. Gustavsson, U. Ståhl, A. Dahlqvist, E. Wiberg, A. Banas, M. Lenman, H. Ronne, and S. Stymne. 2002. Storage Lipid Synthesis Is Non-essential in Yeast. *J. Biol. Chem.* 277:6478–6482. doi:10.1074/jbc.M109109200.

Schmeisser, S., S. Li, B. Bouchard, M. Ruiz, C. Des Rosiers, and R. Roy. 2019. Muscle-Specific Lipid Hydrolysis Prolongs Lifespan through Global Lipidomic Remodeling. *Cell Rep.* 29:4540-4552.e8. doi:10.1016/j.celrep.2019.11.090.

Schmidt, C., K. Athenstaedt, B. Koch, B. Ploier, and G. Daum. 2013. Regulation of the Yeast Triacylglycerol Lipase Tgl3p by Formation of Nonpolar Lipids. *J. Biol. Chem.* 288:19939–19948. doi:10.1074/jbc.M113.459610.

Schmidt, C., K. Athenstaedt, B. Koch, B. Ploier, M. Korber, G. Zellnig, and G. Daum. 2014. Defects in triacylglycerol lipolysis affect synthesis of triacylglycerols and steryl esters in the yeast. *Biochim. Biophys. Acta BBA - Mol. Cell Biol. Lipids*. 1841:1393–1402. doi:10.1016/j.bbalip.2014.07.001.

Schott, M.B., S.G. Weller, R.J. Schulze, E.W. Krueger, K. Drizyte-Miller, C.A. Casey, and M.A. McNiven. 2019. Lipid droplet size directs lipolysis and lipophagy catabolism in hepatocytes. *J. Cell Biol.* 218:3320–3335. doi:10.1083/jcb.201803153.

Shaw, D.E., J.P. Grossman, J.A. Bank, B. Batson, J.A. Butts, J.C. Chao, M.M. Deneroff, R.O. Dror, A. Even, C.H. Fenton, A. Forte, J. Gagliardo, G. Gill, B. Greskamp, C.R. Ho, D.J. Ierardi, L. Iserovich, J.S. Kuskin, R.H. Larson, T. Layman, L.-S. Lee, A.K. Lerer, C. Li, D. Killebrew, K.M. Mackenzie, S.Y.-H. Mok, M.A. Moraes, R. Mueller, L.J. Nociolo, J.L. Peticolas, T. Quan, D. Ramot, J.K. Salmon, D.P. Scarpazza, U.B. Schafer, N. Siddique, C.W. Snyder, J. Spengler, P.T.P. Tang, M. Theobald, H. Toma, B. Towles, B. Vitale, S.C. Wang, and C. Young. 2014. Anton 2: Raising the Bar for Performance and Programmability in a Special-Purpose Molecular Dynamics Supercomputer. *In* SC14: International Conference for High Performance Computing, Networking, Storage and Analysis. IEEE, New Orleans, LA, USA. 41–53.

Sorger, D., K. Athenstaedt, C. Hrastnik, and G. Daum. 2004. A Yeast Strain Lacking Lipid Particles Bears a Defect in Ergosterol Formation. *J. Biol. Chem.* 279:31190–31196. doi:10.1074/jbc.M403251200.

Strande, S., H. Cai, M. Tatineni, W. Pfeiffer, C. Irving, A. Majumdar, D. Mishin, R. Sinkovits, M. Norman, N. Wolter, T. Cooper, I. Altintas, M. Kandes, I. Perez, M. Shantharam, M. Thomas, S. Sivagnanam, and T. Hutton. 2021. Expanse: Computing without Boundaries: Architecture, Deployment, and Early Operations Experiences of a Supercomputer Designed for the Rapid Evolution in Science and Engineering. *In* Practice and Experience in Advanced Research Computing. ACM, Boston MA USA. 1–4.

bioRxiv preprint doi: https://doi.org/10.1101/2023.03.07.531595; this version posted March 7, 2023. The copyright holder for this preprint (which was not certified by peer review) is the author/funder. All rights reserved. No reuse allowed without permission.

Teixeira, V., L. Johnsen, F. Martínez-Montañés, A. Grippa, L. Buxó, F.-Z. Idrissi, C.S. Ejsing, and P. Carvalho. 2018. Regulation of lipid droplets by metabolically controlled Ldo isoforms. *J. Cell Biol.* 217:127–138. doi:10.1083/jcb.201704115.

Thiam, A.R., and M. Beller. 2017. The why, when and how of lipid droplet diversity. *J. Cell Sci.* jcs.192021. doi:10.1242/jcs.192021.

Tribello, G.A., M. Bonomi, D. Branduardi, C. Camilloni, and G. Bussi. 2014. PLUMED 2: New feathers for an old bird. *Comput. Phys. Commun.* 185:604–613. doi:10.1016/j.cpc.2013.09.018.

Tsirigos, K.D., C. Peters, N. Shu, L. Käll, and A. Elofsson. 2015. The TOPCONS web server for consensus prediction of membrane protein topology and signal peptides. *Nucleic Acids Res.* 43:W401–W407. doi:10.1093/nar/gkv485.

Ugrankar, R., J. Bowerman, H. Hariri, M. Chandra, K. Chen, M.-F. Bossanyi, S. Datta, S. Rogers, K.M. Eckert, G. Vale, A. Victoria, J. Fresquez, J.G. McDonald, S. Jean, B.M. Collins, and W.M. Henne. 2019. Drosophila Snazarus Regulates a Lipid Droplet Population at Plasma Membrane-Droplet Contacts in Adipocytes. *Dev. Cell*. 50:557-572.e5. doi:10.1016/j.devcel.2019.07.021.

Walther, T.C., J. Chung, and R.V. Farese. 2017. Lipid Droplet Biogenesis. *Annu. Rev. Cell Dev. Biol.* 33:491–510. doi:10.1146/annurev-cellbio-100616-060608.

Wang, H., M. Becuwe, B.E. Housden, C. Chitraju, A.J. Porras, M.M. Graham, X.N. Liu, A.R. Thiam, D.B. Savage, A.K. Agarwal, A. Garg, M.-J. Olarte, Q. Lin, F. Fröhlich, H.K. Hannibal-Bach, S. Upadhyayula, N. Perrimon, T. Kirchhausen, C.S. Ejsing, T.C. Walther, and R.V. Farese. 2016. Seipin is required for converting nascent to mature lipid droplets. *eLife*. 5:e16582. doi:10.7554/eLife.16582.

Welte, M.A. 2015. Expanding Roles for Lipid Droplets. *Curr. Biol.* 25:R470–R481. doi:10.1016/j.cub.2015.04.004.

Wilfling, F., H. Wang, J.T. Haas, N. Krahmer, T.J. Gould, A. Uchida, J.-X. Cheng, M. Graham, R. Christiano, F. Fröhlich, X. Liu, K.K. Buhman, R.A. Coleman, J. Bewersdorf, R.V. Farese, and T.C. Walther. 2013. Triacylglycerol Synthesis Enzymes Mediate Lipid Droplet Growth by Relocalizing from the ER to Lipid Droplets. *Dev. Cell*. 24:384–399. doi:10.1016/j.devcel.2013.01.013.

Wright, R. 2000. Transmission electron microscopy of yeast. *Microsc. Res. Tech.* 51:496–510. doi:10.1002/1097-0029(20001215)51:6<496::AID-JEMT2>3.0.CO;2-9.

Zhang, S., Y. Wang, L. Cui, Y. Deng, S. Xu, J. Yu, S. Cichello, G. Serrero, Y. Ying, and P. Liu. 2016. Morphologically and Functionally Distinct Lipid Droplet Subpopulations. *Sci. Rep.* 6:29539. doi:10.1038/srep29539.

bioRxiv preprint doi: https://doi.org/10.1101/2023.03.07.531595; this version posted March 7, 2023. The copyright holder for this preprint (which was not certified by peer review) is the author/funder. All rights reserved. No reuse allowed without permission.

1326

bioRxiv preprint doi: https://doi.org/10.1101/2023.03.07.531595; this version posted March 7, 2023. The copyright holder for this preprint (which was not certified by peer review) is the author/funder. All rights reserved. No reuse allowed without permission.

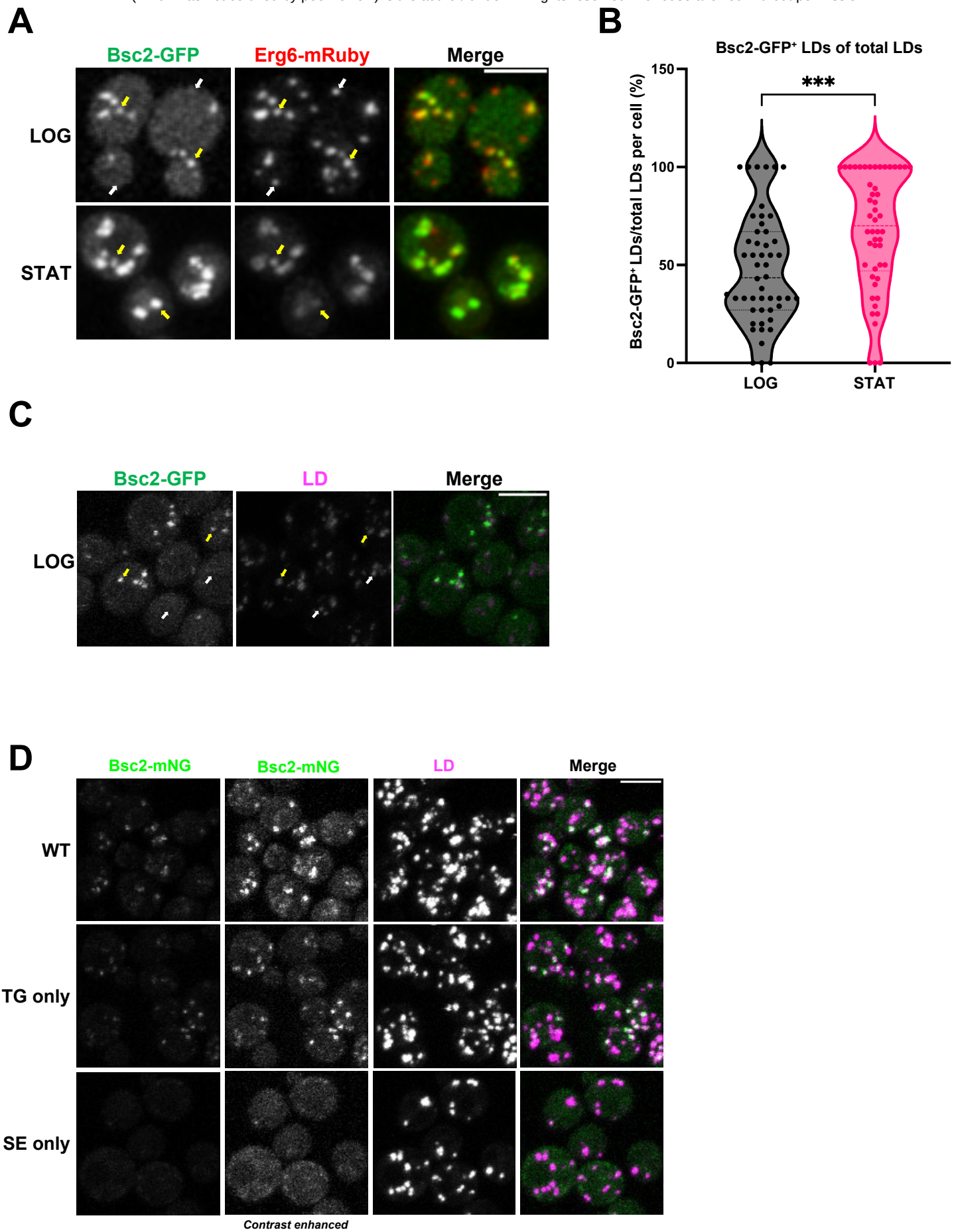

Figure 1

bioRxiv preprint doi: https://doi.org/10.1101/2023.03.07.531595; this version posted March 7, 2023. The copyright holder for this preprint (which was not certified by peer review) is the author/funder. All rights reserved. No reuse allowed without permission.

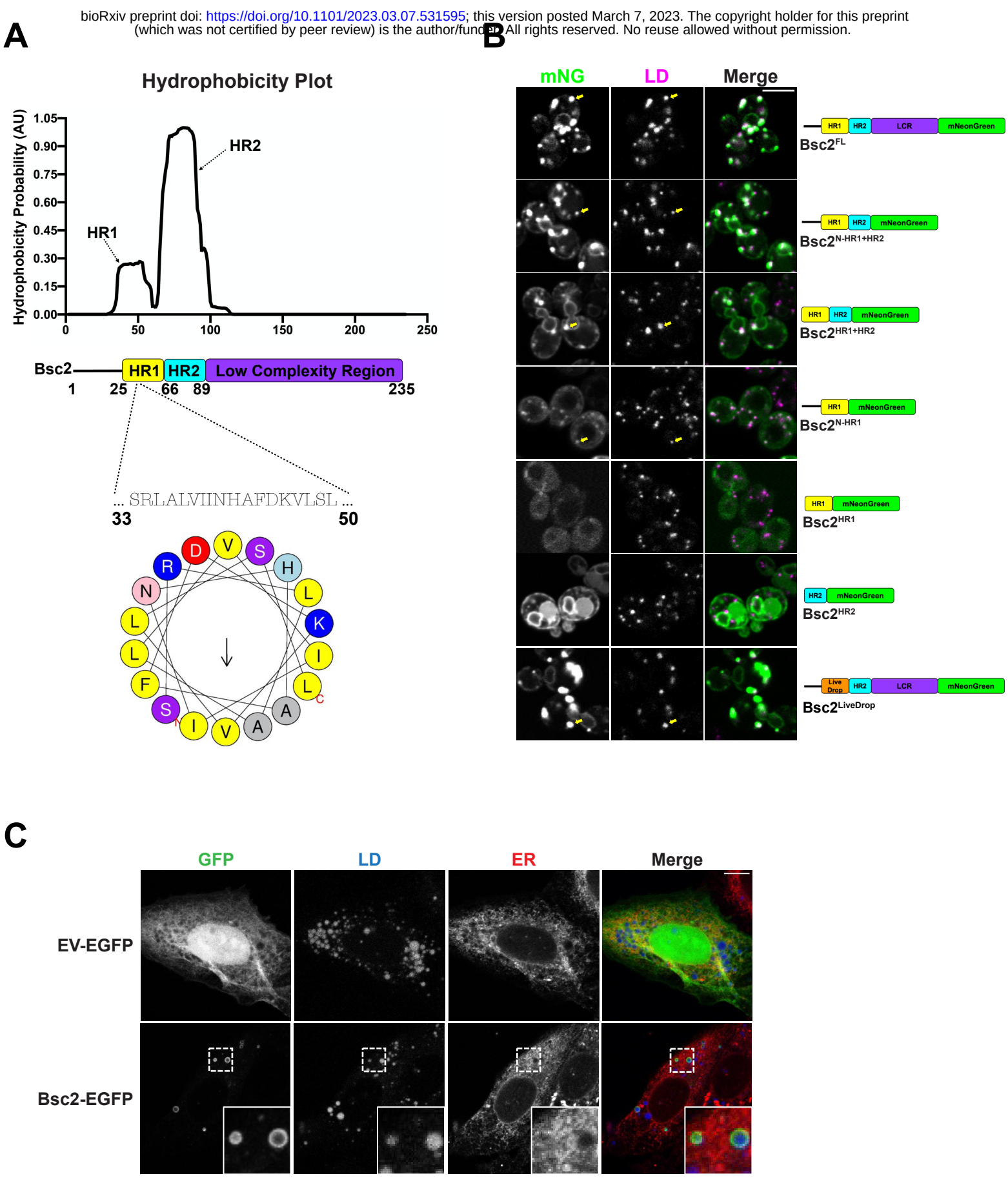

Figure 2

bioRxiv preprint doi: https://doi.org/10.1101/2023.03.07.531595; this version posted March 7, 2023. The copyright holder for this preprint (which was not certified by peer review) is the author/funder. All rights reserved. No reuse allowed without permission.

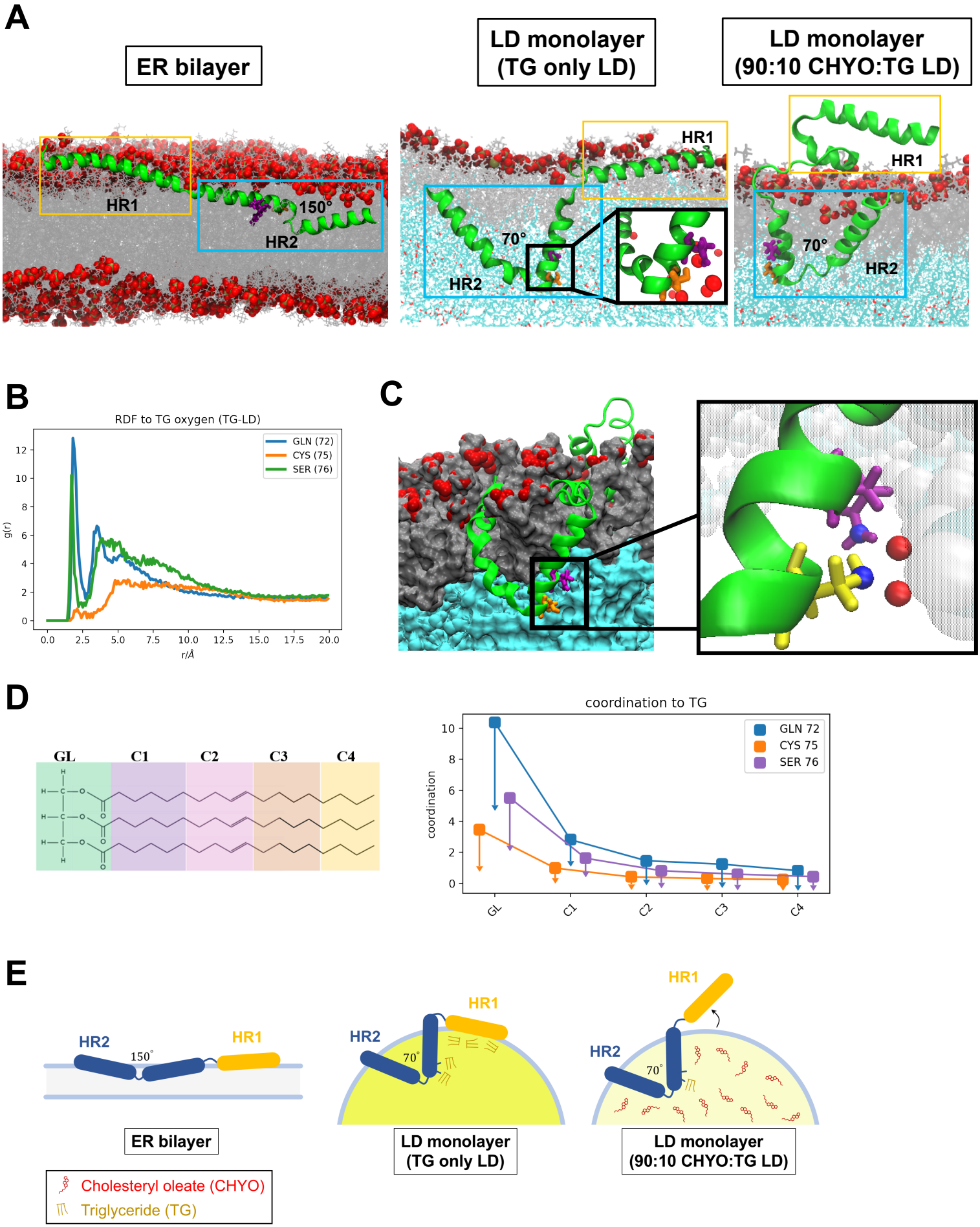

Figure 3

bioRxiv preprint doi: https://doi.org/10.1101/2023.03.07.531595; this version posted March 7, 2023. The copyright holder for this preprint (which was not certified by peer review) is the author/funder. All rights reserved. No reuse allowed without permission.

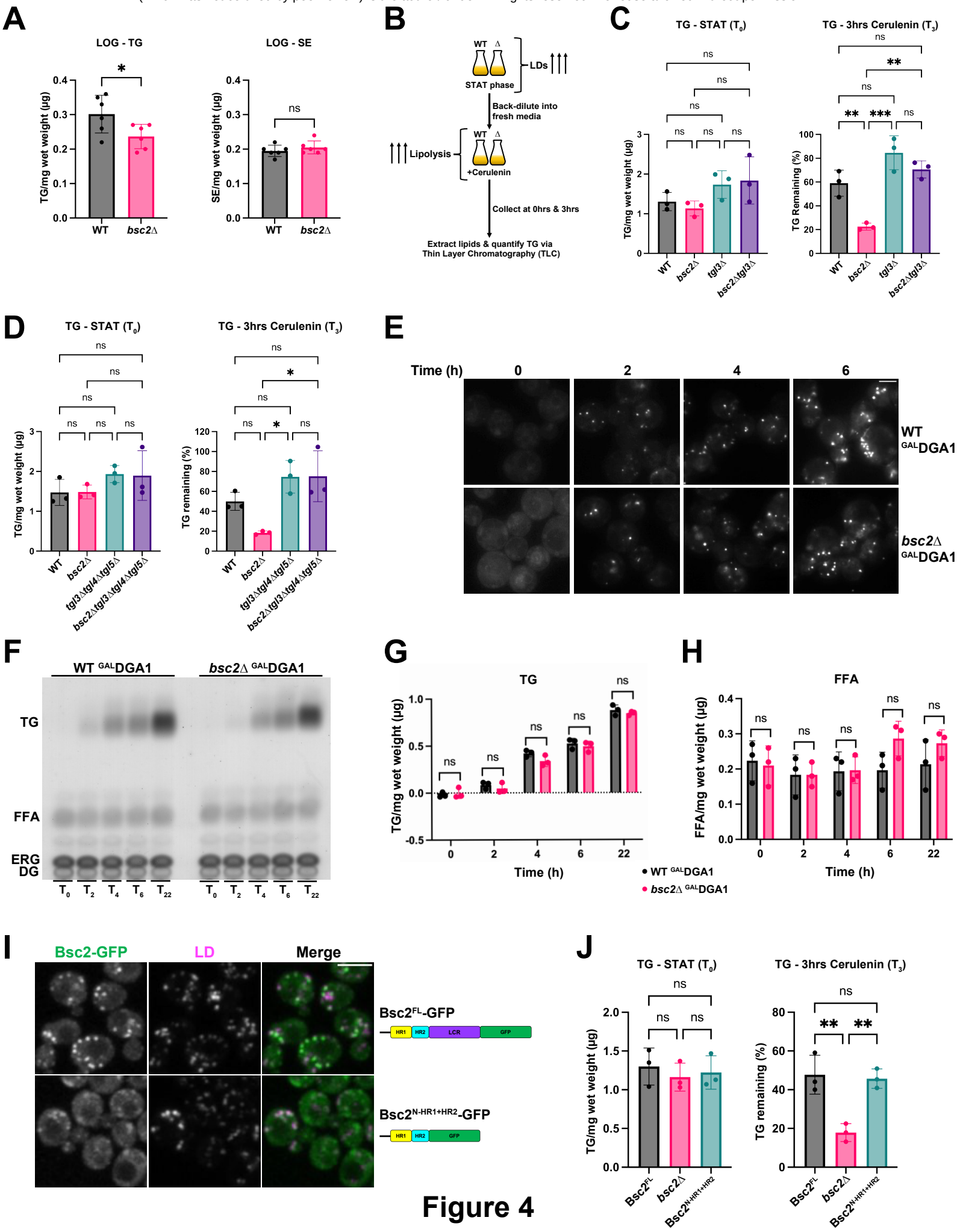

Figure 4

bioRxiv preprint doi: https://doi.org/10.1101/2023.03.07.531595; this version posted March 7, 2023. The copyright holder for this preprint (which was not certified by peer review) is the author/funder. All rights reserved. No reuse allowed without permission.

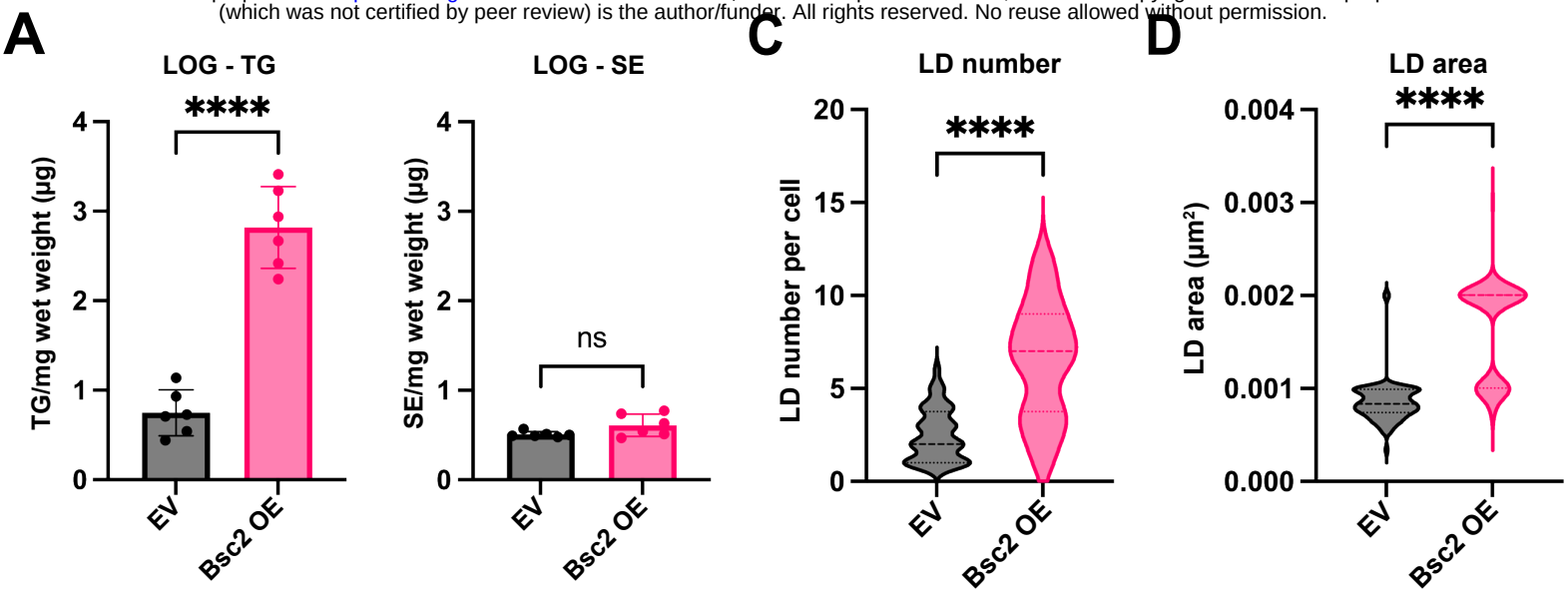

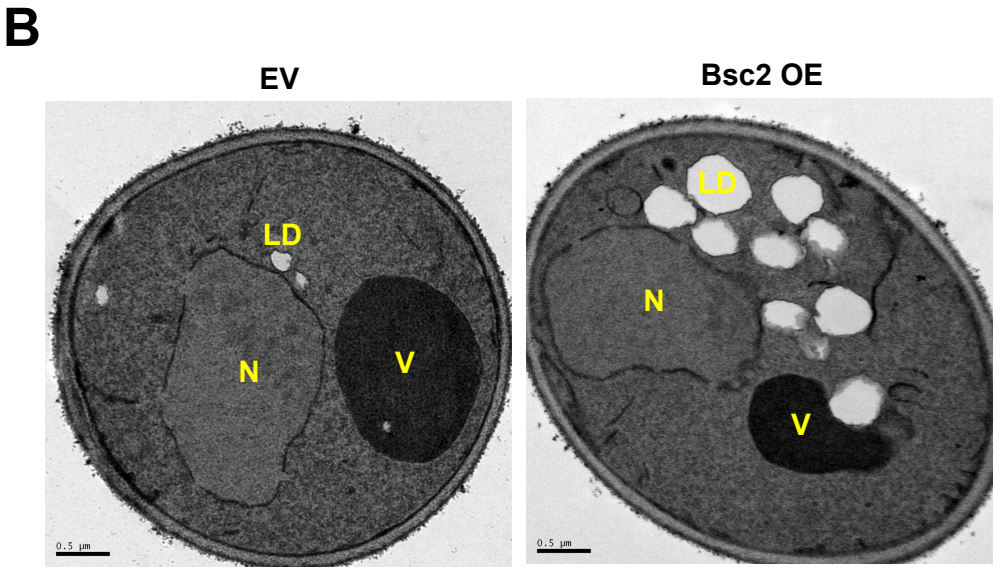

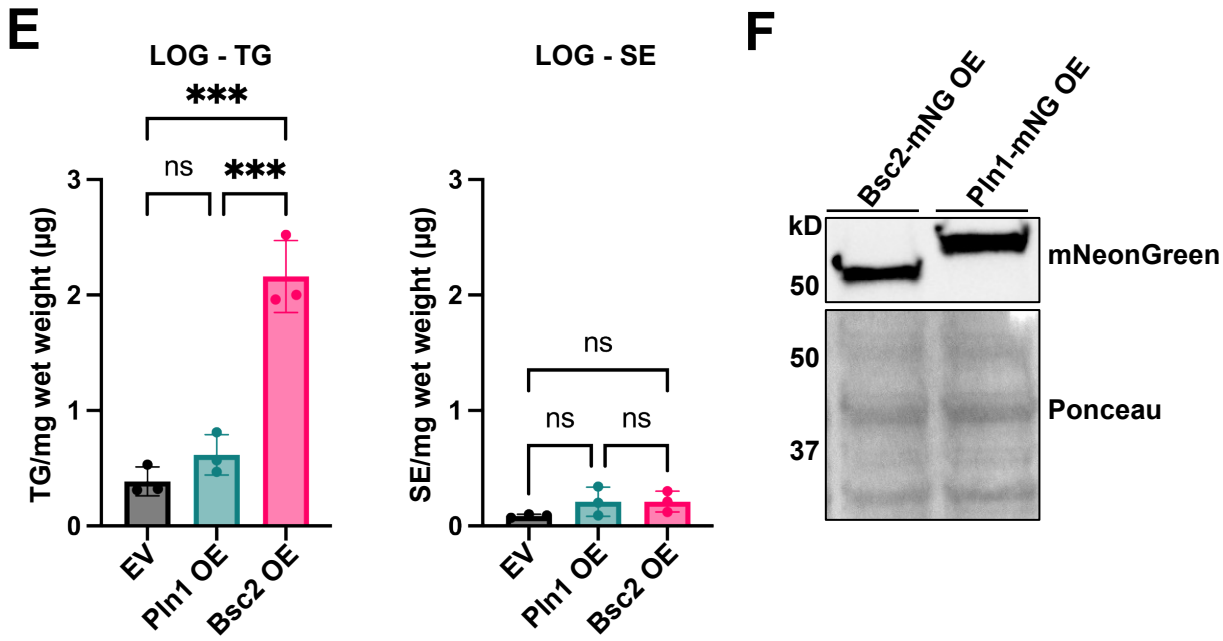

Figure 5

bioRxiv preprint doi: https://doi.org/10.1101/2023.03.07.531595; this version posted March 7, 2023. The copyright holder for this preprint (which was not certified by peer review) is the author/funder. All rights reserved. No reuse allowed without permission.

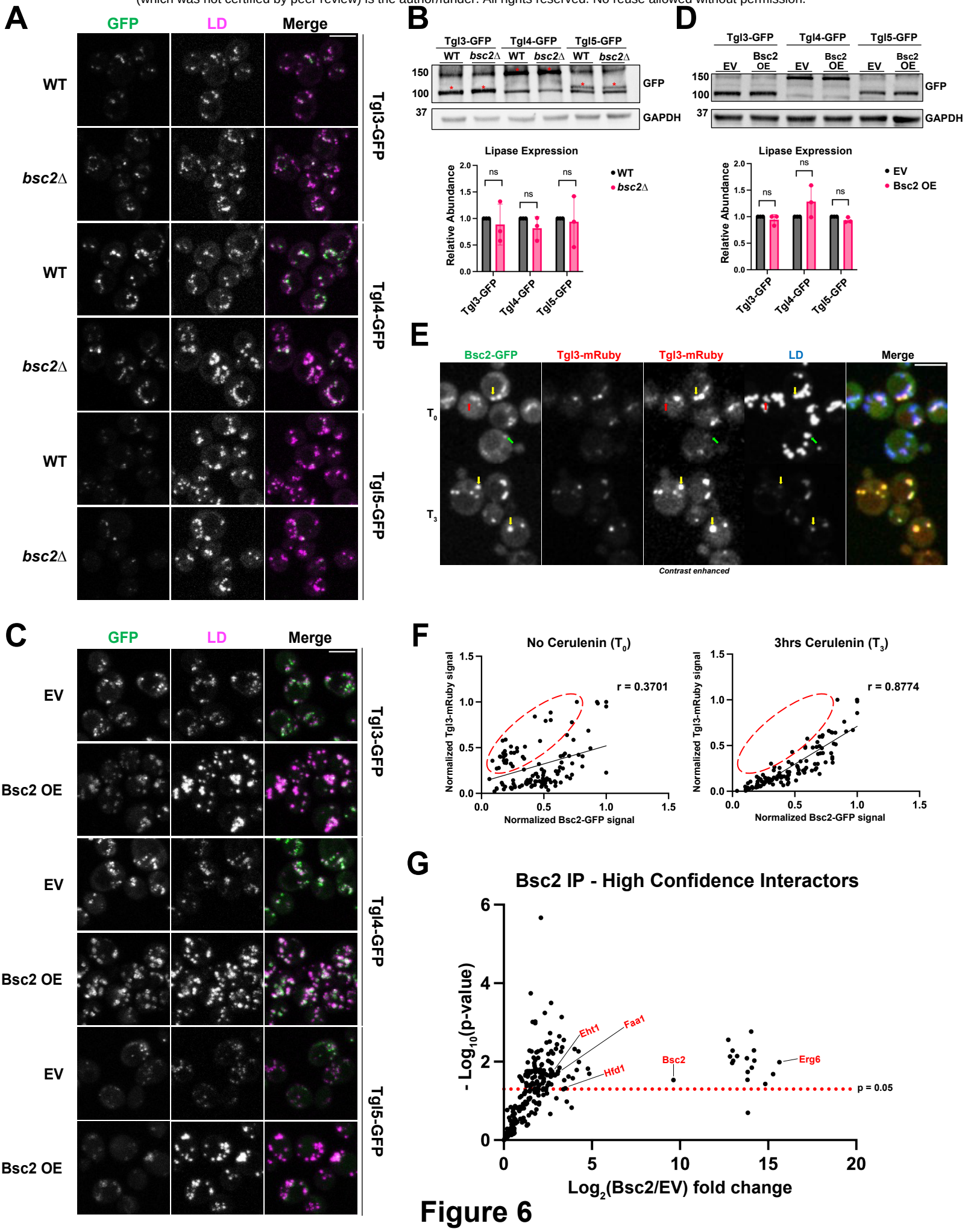

Figure 6

bioRxiv preprint doi: https://doi.org/10.1101/2023.03.07.531595; this version posted March 7, 2023. The copyright holder for this preprint (which was not certified by peer review) is the author/funder. All rights reserved. No reuse allowed without permission.

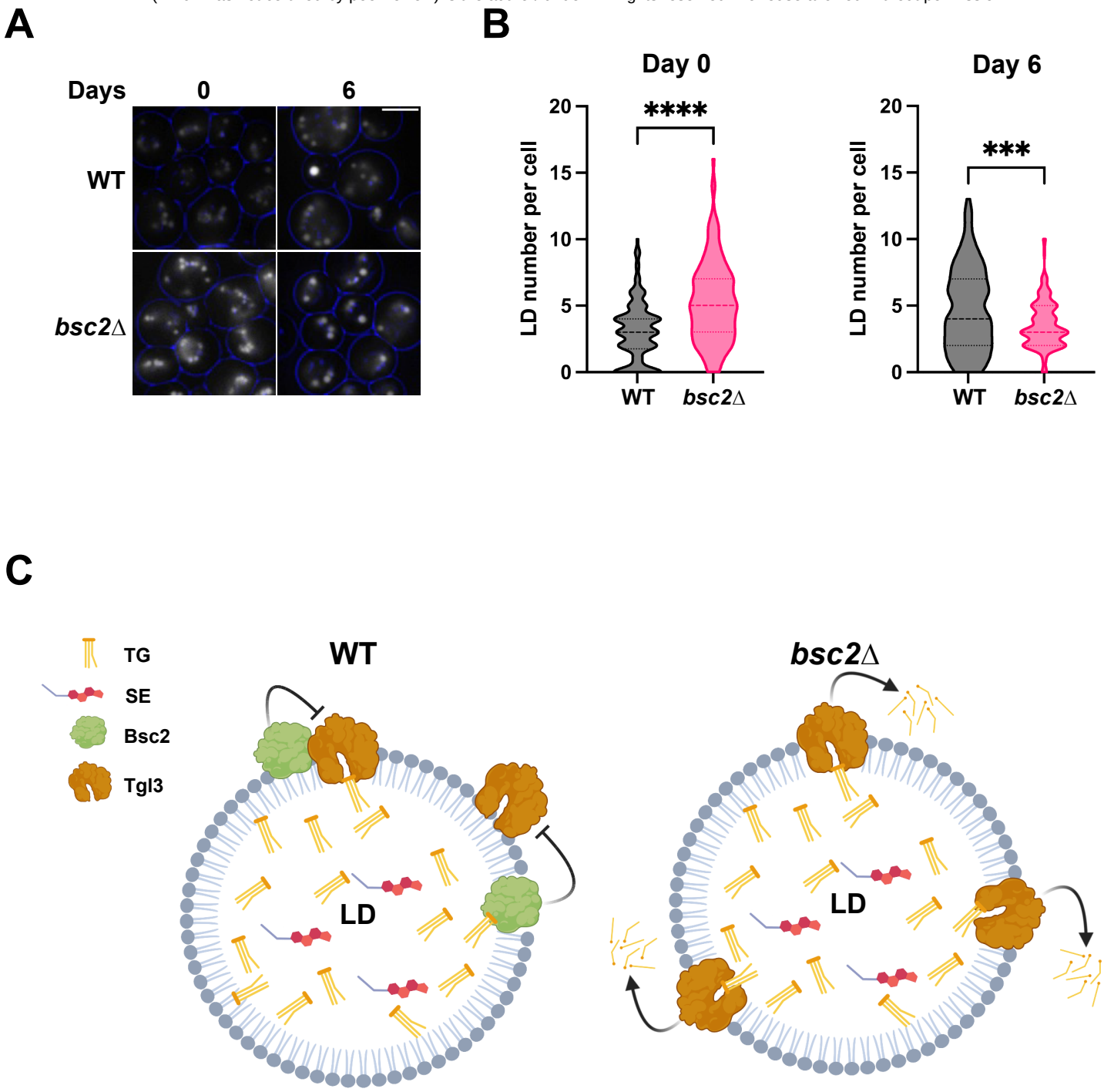

Figure 7

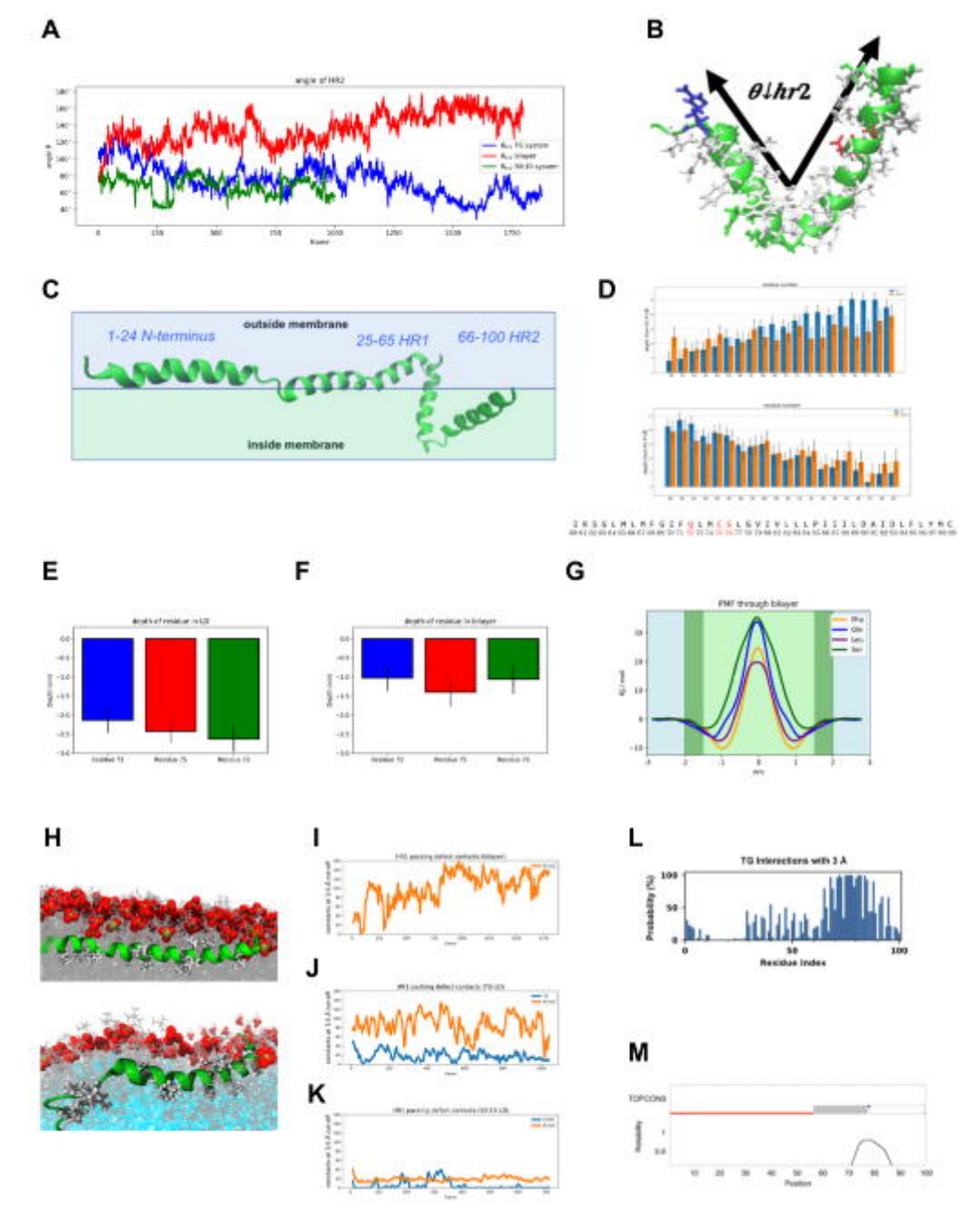
A
angle of HR2
B
θ↓hr2
C
outside membrane
1-24 N-terminus
25-65 HR1
66-100 HR2
inside membrane
D
E
F
G
PMF through bilayer
H
I
J
K
L
TG Interactions with 3 Å
Probability (%)
Residue Index
M
TOPCONS
Position

Figure S3